
Numerical calculations for electronic transport through molecular systems

Robert Dahlke



München 2004

Numerical calculations for electronic transport through molecular systems

Robert Dahlke

Dissertation
der Fakultät für Physik
der Ludwig-Maximilians-Universität
München

vorgelegt von
Robert Dahlke
aus Aachen

München, den 23. April 2004

Erstgutachter: Prof. Dr. Ulrich Schollwöck
Zweitgutachter: Prof. Dr. Axel Schenzle
Tag der mündlichen Prüfung: 8. Juli 2004

Contents

Zusammenfassung	ix
1 Introduction	1
2 Description of charge transport	5
2.1 Perturbative approaches	5
2.1.1 Rate equations	6
2.1.2 Bardeen formula	8
2.1.3 Tersoff-Hamann formula	9
2.1.4 Beyond the Tersoff-Hamann approximation	10
2.2 Scattering approaches	11
2.2.1 Definition of the scattering matrix	11
2.2.2 Landauer-Büttiker formalism	12
3 Quantum-chemical description of nanoscale systems	17
3.1 Ab-initio quantum-chemical methods	18
3.1.1 Separating nuclear and electronic problem	18
3.1.2 Approximations to the electronic problem	19
3.1.3 Approximations to the molecular orbitals	21
3.2 Density functional theory	22
3.2.1 Hohenberg-Kohn formulation of DFT	23
3.2.2 Local density approximation	24
3.2.3 Basis set	25
3.3 Semiempirical methods	25
3.3.1 Overview of methods in use	26
3.3.2 Extended-Hückel method	27
3.3.3 Concluding remarks	29
4 The Elastic-Scattering Quantum-Chemistry Method	31
4.1 Outline of the ESQC algorithm	31
4.1.1 Algorithm step by step	32

4.1.2	Notes on calculations of conductance properties	34
4.1.3	Notes on STM image calculations	35
4.2	Detailed description of ESQC	35
4.2.1	Isolated semi-infinite leads	36
4.2.2	Connecting leads via a molecular region	42
4.2.3	Numerical implementation	45
5	Using molecules as electronic devices	49
5.1	Historical overview	49
5.1.1	Theoretical prediction	49
5.1.2	Experimental realisation	51
5.2	Qualitative model for transport	53
5.3	Recent experiments	54
5.4	Numerical calculations	55
5.4.1	Short summary of recent theoretical studies	56
5.4.2	Conduction properties of PDI devices	57
5.4.3	Discussion	65
6	Understanding STM images	67
6.1	Introduction	67
6.1.1	Historical overview	67
6.1.2	Working principle	68
6.1.3	Examples of STM images	70
6.2	Numerical STM image calculations	71
6.2.1	Image contrast inversion	71
6.2.2	Negative differential resistance	71
6.2.3	Electric field effects	73
6.2.4	Conformational analysis of self-organised monolayers .	75
	Bibliography	81
	Danksagung	91

List of Figures

2.1	Schematic representation of leads and defect	15
2.2	Occupation of energy levels within left and right contact	16
4.1	Partitioning of the system into several parts	32
4.2	Discrete energy levels around the Fermi level	34
4.3	Splitting of the bulk region	37
4.4	Incoming and outgoing wave amplitudes	43
4.5	Graphite unit cell	46
4.6	Super cell of graphite (side view)	47
4.7	Super cell of graphite (top view)	47
5.1	Example for a rectifying molecule	50
5.2	Energy versus distance diagram, no bias	51
5.3	Energy versus distance diagram, forward bias	52
5.4	Energy versus distance diagram, reverse bias	52
5.5	Chemical structures	55
5.6	Structure of Cluster	59
5.7	Structure containing two, three, and four molecules	60
5.8	Spectrum and fit for one to four molecules	61
5.9	Influence of molecular interaction	63
5.10	Influence of molecular interaction 2	64
5.11	<i>IV</i> -calculation	65
6.1	Working principle of an STM	69
6.2	STM-image collection	70
6.3	Image contrast inversion	72
6.4	Influence of tip-induced electric field	74
6.5	Two conformations of the same molecule	75
6.6	STM images of different molecular conformations	76
6.7	Two different conformations	78
6.8	Sample STM image calculations	79

List of Tables

Zusammenfassung

Thema der vorliegenden Arbeit ist die Beschreibung von Ladungstransport-eigenschaften molekularer Systeme, wenn diese das Verbindungsstück zweier Elektroden bilden. Einen technologischen Meilenstein setzte auf diesem Ge-biet die Rastertunnelmikroskopie (Binnig et al., 1981), mit der die gezielte Untersuchung von Transporteigenschaften einzelner, auf Oberflächen adsor-bierter Moleküle möglich ist. Parallel dazu ermöglicht der immense Fort-schritt in der Miniaturisierung klassischer elektronischer Bauteile die Her-stellung von Zuleitungsstrukturen auf der Nanometerskala, die mit einzelnen oder nur wenigen Molekülen überbrückt werden können (Reed et al., 1997). Es besteht die Hoffnung, mit solchen Systemen Schaltungselemente zu rea-lisieren, die heutigen elektronischen Bauteilen in Hinblick auf ihre Effizienz und den Grad ihrer Miniaturisierung deutlich überlegen sein werden.

Experimente mit diesen molekularelektronischen Apparaten werfen die Frage auf, wie sich die chemische Natur eines Moleküls sowie seine Kopplung an die Oberfläche der Elektroden auf die Leitungseigenschaften auswirkt. Eine theoretische Beantwortung dieser Frage erzwingt eine quantenmechani-sche Beschreibung des Systems. Da trotz bedeutender Fortschritte bisher nur beschränkt Übereinstimmung zwischen den Ergebnissen besteht, handelt es sich hierbei um ein aktuelles Gebiet der Grundlagenforschung.

Diese Arbeit beginnt mit einem Überblick über die gängigen Methoden zur theoretischen Beschreibung von Ladungstransport durch molekulare Sy-steme. Anschließend werden Methoden der Quantenchemie behandelt, da diese in nahezu allen Ansätzen zur Beschreibung von elektronischem Trans-port durch molekulare Systeme Anwendung finden.

Auf diese allgemeinen Darstellungen folgt eine detaillierte Beschreibung des numerischen Verfahrens, das im Rahmen dieser Dissertation implemen-tiert worden ist. Mit der vorliegenden Arbeit wird eine Verallgemeinerung der ursprünglichen Methode eingeführt, die vormalige Einschränkungen bezüglich der betrachtbaren Systeme erfolgreich beseitigt.

Diese erweiterte Methode wird dann verwendet, um der durch Experimen-te von Dupraz, Beierlein und Kotthaus (2003) aufgekommenen Frage nachzu-gehen, welchen Einfluß verschiedene geometrische Anordnungen einer Gruppe von identischen Molekülen auf die Leitfähigkeitseigenschaften eines moleku-larelektronischen Apparats ausüben. Unsere Untersuchungen zeigen, daß sich die Transporteigenschaften nur bei Bildung von Molekülgruppierungen mit bedeutender intermolekularer Wechselwirkung wesentlich von denen einzel-ner Moleküle unterscheiden. Damit können wir Konsequenzen für die Re-produzierbarkeit gewonnener Meßdaten aus der Stabilität der Verbindung zwischen Molekül und Elektroden ableiten.

Abschließend befassen wir uns mit der Berechnung von Rastertunnelmikroskop-Bildern und präsentieren eigene Rechnungen, die im Rahmen einer Kooperation mit Constable, Hermann et al. (2004) durchgeführt werden. Durch einen Vergleich mit experimentellen Bildern sollen verschiedene Konformationen eines auf Graphit adsorbierten Moleküls identifiziert werden. Die enorme Größe des Moleküls führt zu einer Gesamtsystemgröße, die eine numerische Durchführung der Algorithmen in der Praxis bisher scheitern ließ. Durch eine von uns eingeführte neuartige Berechnung sind wir in der Lage, erstmalig weitaus größere Systeme zu betrachten, als dies bisher möglich war.

Chapter 1

Introduction

The subject of this thesis is the description of charge transport properties of molecular systems, bridging two electrodes. Although electrical phenomena were already known to the Ancient Greeks, systematic studies regarding stationary charge transport (i.e. electrical current) had not been possible until the year 1800, when Alessandro Volta succeeded in building the prototype of today's batteries. Shortly after Thomson (1897) discovered the electron, Drude (1900a,b) gave the first atomic model for electrical conduction by describing the electrons in a metal according to the kinetic theory of gases. Despite its success in explaining many observations, some properties of metals measured at low temperatures, like the specific heat, drastically disagree with the predictions of the model. The underlying classical concepts proved to be causing the disagreement. Therefore, detailed descriptions of charge transport need to be based on quantum mechanics. In particular, this is true when transport through individual molecules is considered.

Experimentally, it has not been possible to measure the transport properties of single molecules until about 20 years ago. The major difficulty was – and still is – the controlled attachment of an individual molecule to metallic or semiconducting leads, which is however necessary to apply a bias voltage. With the advent of scanning tunnelling microscopy, this type of measurements became feasible for the first time. Originally developed for obtaining topographic surface images with atomic resolution (Binnig et al., 1981), selective studies of transport properties of individual molecules adsorbed on surfaces can now be performed. Parallel to this development, the tremendous advances in fabricating increasingly smaller semiconductor devices together with experiments on self-assembling molecules, render it possible to build lead contacts on the nanometer scale, which can be bridged by single or few molecules (Reed et al., 1997). There is hope for the realisation of circuit elements, built from such systems, which outclass today's electronic circuits

with respect to both efficiency and miniaturisation.

As of today, this is still a field of intense fundamental research, the reason being twofold: at first, the fabricated devices still lack reproducibility mainly because the deposition of molecules has to be performed in an uncontrollable fashion. Secondly, the impact on the measured conductance properties due to both the chemical nature of the molecule itself and its bonding to the lead surface is not consistently understood.

Because of this lack of understanding, intense theoretical studies go along with the experiments. The ultimate aim is to correlate the molecular electronic structure with the conduction properties in a predictive manner, which would be a crucial step towards a directed design of molecular electronic devices.

This thesis is organised in the following way. In Chap. 2 we start by addressing the question of how one can describe current across a molecular system, attached to a source and a drain lead. An overview of well-established theoretical methods for dealing with this problem is given. We characterise them in terms of underlying assumptions and applied approximations. In particular, we distinguish between two types of approaches, perturbative ones and those based on scattering theory. Among the perturbative methods, we discuss the Tersoff-Hamann formula which gave the first theoretical explanation of scanning-tunnelling microscope images by relating them to the local density of states of the substrate surface. We then motivate why it is necessary to go beyond this approximation which leads us to the scattering approaches. They have in common that charge transport is attributed to the scattering from incoming electron waves to outgoing ones. This interpretation is known as the Landauer-Büttiker formalism which we describe in detail.

Next, we are concerned with the methods of quantum chemistry, as they provide means of describing molecular systems with respect to their atomic composition. This is why they are involved in almost any description of electronic transport through molecular systems. In a sense they are the counterpart to so-called model Hamiltonians, the usual starting points in mesoscopic physics, which more or less completely ignore the material specific part of a system and are simple enough to allow for a proper many-body treatment. Quantum chemical methods, in contrast, take position and chemical nature for each atom of the system into account, which results in complicated Hamiltonians and therefore require a trade-off regarding the many-body nature of the problem to be made. One distinguishes ab-initio, density-functional and semiempirical methods, each of which category is outlined in Chap. 3 with special attention to the approximations involved.

Following this general part, a detailed presentation of the numerical

method we have implemented for the study of charge transport through molecular systems is given in Chap. 4. It is based on the so-called *elastic-scattering quantum-chemistry* method, which was introduced by Sautet and Joachim (1988a). Originally, the method was derived in a one-dimensional context, and although it was later extended to three dimensions, an anomaly of the one-dimensional case gave rise to a restriction of the systems which one was able to study. With this thesis, a proper three-dimensional generalisation of the method is introduced. By a thorough treatment of the underlying scattering problem, we are able to lift the former restriction. In addition to that, our generalised method is numerically more stable.

The remainder of this thesis is then devoted to the application of theoretical methods to specific experimental situations. Content of Chap. 5 are molecular electronic devices. We address the question raised by the experiments of Dupraz et al. (2003), how the conductance properties of a molecular electronic device are influenced by a change in the geometrical alignment of the molecules bridging the electrodes. Our analysis reveals that the transport properties of a group of identical molecules differ from those of a single molecule only when inter-molecular interactions are considerably large. In particular, for those inter-molecular distances which are to be expected for typical self-assembled monolayers, such an effect does not occur. Only for molecular clusters with distances almost as small as atomic distances, a significant change in the conduction properties is observed. These clusters represent defects in the monolayer and can be produced when the coupling between molecules and lead surface is sufficiently weak. The strength of the coupling mainly depends on the chemical type of the molecular group which is responsible for the adsorption to the leads.

In Chap. 6 we consider scanning tunnelling microscope image calculations. After an introduction to the working principle of the device, we review recent numerical studies which proved to be necessary in order to interpret experimental image data correctly. Then we present our own calculations from a cooperation with Constable et al. (2004) to support the interpretation of recent STM images. The goal of the experiment is to identify different possible conformations for a molecule when adsorbed on graphite. As the system under investigation is considerably large, we were able to produce the numerical images only by introducing a special treatment for a large eigenvalue problem, which cannot be solved sufficiently accurately by conventional methods. This is the first time that a method has been implemented that can perform image calculations for a system of that size.

Chapter 2

Description of charge transport

The problem which we address in this chapter can be stated as follows: how to describe current across a molecular system, when it is attached to a source and a drain lead both having different chemical potentials? To this end the theoretical methods which are in use for modelling electron tunnelling in molecular systems are surveyed. These methods can be divided into two categories: the ones which are based on perturbation theory and the ones which apply scattering theory.

Within the first category the solution for one part of the system is assumed to be known. Charge transport is described as the transition between such known states due to the influence of the rest of the system, which constitutes the perturbing potential or enters via tunnelling matrix elements.

Scattering approaches take solutions to the entire system and distinguish between incoming states which move in direction of the molecular region and outgoing states which move away from it. Charge transport is attributed to the scattering from in-states to out-states. This interpretation is known as the Landauer-Büttiker formalism.

In this chapter we first deal with perturbative methods, among which we distinguish two different approaches. Then we turn to scattering methods of which we discuss the basic principles. A full explanation of the approach we have implemented, which belongs to the latter type, is deferred to Chap. 4.

2.1 Perturbative approaches

The central element of perturbation theory is a so-called unperturbed system Σ_0 , described by a Hamiltonian H_0 , for which one is in principle able to obtain the eigenfunctions and eigenenergies exactly. This system is then perturbed by an interaction Hamiltonian H_{int} and this interaction is assumed to be small

as compared to the energy scales of the unperturbed system, so that one can expand its influence into a converging power series. We refer to schemes which follow this classic form of perturbation theory as rate-equation approaches (Sec. 2.1.1). Within those H_0 describes the molecular region only while H_{int} describes the coupling to the leads.

All subsequent perturbative methods take a different viewpoint. There the unperturbed system consists not only of a single system but of two systems (called Σ_1 and Σ_2 corresponding to source and drain lead¹) which do not interact with each other. They are described by the Hamiltonians H_1 and H_2 . The molecular region plays the role of the perturbing potential. Ordinary perturbation theory can not be applied because the eigenfunctions for both systems are not orthogonal. To overcome this problem one uses an approach which relates back to Bardeen (1961) and is the content of Sec. 2.1.2. With only a few further assumptions the Tersoff-Hamann formula (Sec. 2.1.3) can be derived, which historically constitutes the first theoretical interpretation of STM images. Finally we remark on methods going beyond the Tersoff-Hamann approximation.

2.1.1 Rate equations

As mentioned in the introduction this first approach to electron transport differs from the following ones because the unperturbed system Σ_0 consists of a single molecule only, while the interaction part represents a connection to the leads. It can therefore not be applied to STM image calculations, because a molecular adsorbate can not be described without the substrate surface and furthermore, as an adsorbed molecule is hardly ever weakly coupled to the substrate, perturbation theory is not applicable. Therefore this method has only been used to calculate conductance properties of single molecules, assuming a situation of weak coupling to the leads (Hettler et al., 2002, 2003). Charge transport is related to the transition of electronic states from the molecular system Σ_0 to states within the leads, due to the action of the coupling.

Since within this approach one first treats the molecular system as being isolated from the leads, it has the advantage that it allows for a detailed many-particle description. The presentation follows Hettler et al. (2002).

¹We have chosen numerical subscripts (instead of e.g. L and R for left and right lead) because they can easily be extended to more than two leads.

The Hamiltonian

We think of the entire system as being divided into three parts, the molecular system Σ_0 , as well as two leads. The total Hamiltonian reads

$$H = H_0 + H_{\text{int}}, \quad (2.1)$$

where the isolated molecular part is described by H_0 and the interaction part by H_{int} , which couples the molecule to the leads.

The molecular region is treated from a many-particle point of view and therefore correlation effects can properly be accounted for by including two-body operators in H_0 . One of the well established tools for diagonalising such a Hamiltonian like direct numerical diagonalisation can be used to obtain both its spectrum and the corresponding electronic eigenfunctions.

The coupling term H_{int} merely consists of hopping terms from the lead to the molecule and vice versa. To be specific, the interaction Hamiltonian is supposed to be of the form

$$H_{\text{int}} = \sum_{l=1,2} \left(\frac{\Gamma}{2\pi\rho_e} \right)^{1/2} \sum_{\mathbf{k}\sigma i} \left(t_i^l c_{i\sigma}^\dagger a_{l\mathbf{k}\sigma} + \text{h.c.} \right), \quad (2.2)$$

where the operators $c_{i\sigma}, c_{i\sigma}^\dagger$ destroy and create electrons with spin σ in state i of the molecule and the operators $a_{l\mathbf{k}\sigma}, a_{l\mathbf{k}\sigma}^\dagger$ act correspondingly in the leads ($l = 1, 2$), with a dispersion relation $E(l\mathbf{k}\sigma) = E_{\mathbf{k}}^l$. The density of states in the leads ρ_e is assumed to be constant. The parameters t_i^l account for a variable coupling between the individual states. The interaction Hamiltonian can be extended to also include a coupling to bosonic degrees of freedom (i.e. photons and/or phonons), which we do not consider here for simplicity reasons (see Hettler et al., 2002).

Master equation

With the diagonalisation of H_0 obtained, a master equation is set up for the occupation probabilities P_s of the molecular many-body states. Transition rates can then be calculated using perturbation theory with respect to the coupling constant Γ .

The transition rate $w_{ss'}$ between two molecular states s, s' is composed of the tunnelling rates $w_{ss'}^{l\pm}$ for electrons tunnelling from lead l to the molecule (+) or in the other direction (-), respectively:

$$w_{ss'} = \sum_l (w_{ss'}^{l+} + w_{ss'}^{l-}). \quad (2.3)$$

These tunnelling rates can be computed using the golden rule:

$$w_{ss'}^{l\pm} = \frac{2\pi}{\hbar} \left| \sum_{\phi_l \phi'_l} \langle \phi'_l | \langle s' | H_{\text{int}} | \phi_l \rangle | s \rangle \delta(E_{\phi_l} + E_s - E_{\phi'_l} - E_{s'}) \right|^2, \quad (2.4)$$

with $|\phi_l\rangle$ denoting states in lead l . If these lead states are assumed to be occupied according to a Fermi function $f_l(E)$, then one can replace the expression $|\sum_{\phi_l \phi'_l} \langle \phi'_l | a_{l\mathbf{k}\sigma}^\dagger | \phi_l \rangle|^2$ by $f_l(E_{\mathbf{k}}^l) \rho_e$ and $|\sum_{\phi_l \phi'_l} \langle \phi'_l | a_{l\mathbf{k}\sigma} | \phi_l \rangle|^2$ by $[1 - f_l(E_{\mathbf{k}}^l)] \rho_e$. The in- and out-tunnelling rates thus become

$$w_{ss'}^{l+} = \frac{\Gamma}{\hbar} f_l(E_s - E_{s'}) \sum_{\sigma} \left| \sum_i t_i^l \langle s | c_{i\sigma}^\dagger | s' \rangle \right|^2, \quad (2.5)$$

$$w_{ss'}^{l-} = \frac{\Gamma}{\hbar} [1 - f_l(E_s - E_{s'})] \sum_{\sigma} \left| \sum_i t_i^l \langle s | c_{i\sigma} | s' \rangle \right|^2. \quad (2.6)$$

To obtain a stationary solution for the occupation probabilities P_s of the molecular states, they have to fulfil the following master equation

$$\dot{P}_s = 0 = \sum_{s'} (w_{ss'} P_{s'} - w_{s's} P_s). \quad (2.7)$$

Solving this system of equations yields the occupation probabilities P_s . Now the current from the molecule into one of the leads (say l) is proportional to the net transition of states:

$$I_l = e \sum_{ss'} (w_{ss'}^{l+} P_{s'} - w_{s's}^{l-} P_s). \quad (2.8)$$

In summary we note that this approach for calculating the current can be used to treat the molecular system in great detail. This is achieved by treating the surface of the leads, which are by themselves very complicated objects, as a simple perturbation to the molecular Hamiltonian. Therefore the method is limited to the condition of weak coupling.

2.1.2 Bardeen formula

Now we change the viewpoint and consider two isolated systems, which do this time correspond to macroscopic bulk material, i.e. the leads. Bardeen (1961) addressed this problem by considering two sets of states, which in the case of STM correspond to states in the isolated substrate together with an adsorbate and the isolated STM tip. These states each solve the Schrödinger

equation in their part of the system only. The matrix element for the transition of a state Ψ_μ in the one region to a state Ψ_ν in the other region is given by

$$M_{\mu\nu} = \int \Psi_\mu^* [H - E_\nu] \Psi_\nu d^3r. \quad (2.9)$$

In ordinary perturbation theory $(H - E_\nu)\Psi_\nu$ would reduce to the perturbing potential $V_{\text{int}}\Psi_\nu$. Here the situation is different: there is no perturbing potential and therefore the expression $(H - E_\nu)\Psi_\nu$ vanishes in that part of the system where Ψ_ν solves the Schrödinger equation, but it is non-zero in the other part of the system.

By partial integration, Bardeen was able to show that the expression in Eq. (2.9) is proportional to the current operator applied to the states Ψ_μ and Ψ_ν :

$$M_{\mu\nu} = -\frac{\hbar^2}{2m} \int_S [\Psi_\mu^* \nabla \Psi_\nu - \Psi_\nu \nabla \Psi_\mu^*] d^2r, \quad (2.10)$$

where S is an arbitrary surface lying entirely within the barrier region separating the two systems. (The operator defined by the matrix elements $M_{\mu\nu}$ is referred to as the transfer Hamiltonian.)

Because the matrix element of the transition is proportional to the matrix element of the current operator, it is justified to write the rate of tunnelling from state μ to state ν as:

$$\Gamma_{\mu\nu} = \frac{2\pi}{\hbar} |M_{\mu\nu}|^2 \delta(E_\mu - E_\nu). \quad (2.11)$$

This is the so-called Bardeen formula.

Although the Bardeen formula was originally derived in the context of superconducting tunnelling, it became of great importance for the first interpretations of STM images, due to the work of Tersoff and Hamann.

2.1.3 Tersoff-Hamann formula

By applying the Bardeen formula to the case of STM imaging, Tersoff and Hamann were able to show that the tunnelling current of an STM is proportional to the surface local density of states (LDOS) at the position of the tip evaluated at the Fermi energy (Tersoff and Hamann, 1983, 1985). This famous result is obtained under the following assumptions: firstly perturbation theory in the tip-sample interaction must be applicable, secondly the applied bias voltage as well as the temperature must be low, and finally the entire tip is considered to be merely a point probe.

The derivation is straightforward. Starting from Eq. (2.11), the current between tip and sample is related to the tunnelling matrix elements between eigenstates of these two systems:

$$I = \frac{2\pi e}{\hbar} \sum_{\mu,\nu} f(E_\mu)[1 - f(E_\nu + eV)] |M_{\mu\nu}|^2 \delta(E_\mu - E_\nu), \quad (2.12)$$

with

$$M_{\mu\nu} = \langle \Psi_\mu | V_{\text{tip}} | \Psi_\nu \rangle.$$

Assuming low temperature and low voltage Eq. (2.12) can be approximated as

$$I = \frac{2\pi}{\hbar} e^2 V \sum_{\mu,\nu} |M_{\mu\nu}|^2 \delta(E_\mu - E_F) \delta(E_\nu - E_F). \quad (2.13)$$

If the tip is simply taken to be a point probe located at r_0 , then the tunnelling matrix element reduces to $\Psi_\mu(r_0)$ and one arrives at the Tersoff-Hamann formula:

$$I \propto \sum_{\mu} |\Psi_\mu(r_0)|^2 \delta(E_\mu - E_F). \quad (2.14)$$

2.1.4 Beyond the Tersoff-Hamann approximation

The analytical expression (2.14) is appealing as it relates an STM image directly to the surface electronic structure (note that it is not the electronic density, as Eq. (2.14) is evaluated at the Fermi energy only). However there are situations where the underlying assumptions are not justified.

First of all it may be too crude to entirely neglect the electronic structure of the tip, for example when it has a substantial spatial modulation. Such situations are not well described by the Tersoff-Hamann formula, which assumes an s-state for the tip orbital. In these cases, the Bardeen formula (Eq. 2.11) has to be evaluated numerically. This has been done for example by Tsukada et al. (1990), who performed separate electronic structure calculations for substrate and tip with an ab-initio method. Chen (1990a,b) has studied the influence of STM tips, for which a d-type orbital dominates the tunnelling process.

More severely, whenever a perturbative approach is questionable, the Bardeen formula can not be applied at all. Perturbation theory most obviously fails in describing situations where the STM tip is used to actively manipulate the sample surface. For example, it is possible to remove individual molecules, adsorbed on the sample surface, by lowering the tip-surface distance at the position of that molecule below a certain critical value. Apart

from these extreme cases, perturbation theory is considered to become inaccurate long before the onset of such irreversible effects, i.e. for distances larger than those being involved in manipulation experiments.

Thus, there are relevant cases where perturbation theory itself breaks down and alternative frameworks then have to be used which do not rely on weak coupling between parts of the system but treat the system as a single entity. This will be considered in the next section.

2.2 Scattering approaches

To go beyond perturbation theory, where the tip influence is viewed as perturbing the bulk potential and vice versa, it is necessary to treat the entire system containing tip and sample (for STM calculations) or containing molecule and leads (for conductance calculations of molecules) in a unified way. One possible such framework is scattering theory (see e.g. Taylor, 1972).

To our knowledge, all non-perturbative theories for the STM imaging process solve the scattering problem in the single-particle approximation (Lucas et al., 1988; Sautet and Joachim, 1991; Doyen et al., 1993; Ness and Fisher, 1997). This is because one needs a description of the system which accounts for small geometrical changes (i.e. movement of the tip). Explicit many-particle formalisms are based on model Hamiltonians which contain parameters that cannot be directly obtained from the spatial arrangement of the system. They are therefore not suited for our purpose and we restrict ourselves to the single-particle approximation, too.

2.2.1 Definition of the scattering matrix

For the purpose of scattering theory, it is useful to decompose the system into a bulk region containing the leads (described by the Hamiltonian H_{lead}) and a defect region, being described by an external potential $V(x)$. This defect region has to be spatially localised, and its external potential $V(x)$ (due to atomic cores and external fields if present) has to drop sufficiently fast [$V(x) \sim \mathcal{O}(|x|^{-p})$, for $|x| \rightarrow \infty$ and $p > 1$].

Now consider a wave packet approaching the defect region, yet being far away from it. Its wave function $\Psi_0(x, t_0)$ can be expressed in terms of free solutions $\phi_{\mathbf{k}}$, i.e. in eigenstates of H_{lead} (Bloch waves in our case). To be specific, let its representation in terms of $\phi_{\mathbf{k}}$ be

$$\Psi_0(x, t_0) = \int d^3k a_{\mathbf{k}} \phi_{\mathbf{k}}(x), \quad (2.15)$$

with $a_{\mathbf{k}}$ peaked around some \mathbf{k}_0 . In this representation, the time evolution of Eq. (2.15) will assume a very complicated form once the wave packet enters the scattering region. However, one can define scattering states, which are eigenstates of the full Hamiltonian $H = H_{\text{lead}} + V$ and therefore stationary in time. The wave packet can also be expanded in terms of these scattering states and it can be shown that there exists a special choice these scattering states $\psi_{\mathbf{k}}^{\text{in}}$ (called in-states) for which the wave packet expansion coefficients $A_{\mathbf{k}}$ are identical to those of the expansion in terms of free solutions ($A_{\mathbf{k}} = a_{\mathbf{k}}$). Therefore, as long as t_0 is in the distinct past one has:

$$\Psi_0(x, t_0) = \int d^3k a_{\mathbf{k}} \psi_{\mathbf{k}}^{\text{in}}(x). \quad (2.16)$$

A corresponding relation between free solutions and so-called out-states (which are also eigenstates to $H = H_{\text{lead}} + V$) can be established by considering a wave packet moving away from the defect region. In this sense, any free solution to H_{lead} is asymptotically equal to a scattering state (solution to $H = H_{\text{lead}} + V$).

The scattering problem can be formulated in the following way: How do eigenstates of H_{lead} evolve under the action of $H = H_{\text{lead}} + V$? Put in other words: what is the probability amplitude of an incoming wave packet peaked around \mathbf{k} to evolve into an outgoing one peaked around \mathbf{k}' due to the action of V ? This information is contained in the scattering matrix. Any eigenstate $\phi_{\mathbf{k}}$ to H_{lead} is asymptotically equal to an in-state $\psi_{\mathbf{k}}^{\text{in}}$. This in-state is an eigenstate to the full Hamiltonian $H_{\text{lead}} + V$ and can also be expressed in the basis of out-states. This basis transformation is described by the scattering matrix:

$$|\psi_{\mathbf{k}_0}^{\text{out}}\rangle = S \cdot |\Psi_{\text{in}}\rangle. \quad (2.17)$$

As each out-state is again asymptotically equal to a free solution of H_{lead} , the scattering matrix describes in which way incoming free solutions are scattered into outgoing ones due to the action of V . The details of the scattering problem we are interested in together with a derivation of the scattering matrix directly from the Schrödinger equation is presented in Chap. 4.

The remaining question is how to obtain transport properties once the scattering matrix is known. This will be described in the next section.

2.2.2 Landauer-Büttiker formalism

Within the Landauer-Büttiker formalism (Büttiker et al., 1985), current is described as a result of electron transmission through an impurity region in a single electron picture. This concept is presented here. We first consider

a single narrow conductor placed between two big contacts and derive the quantisation of conductance. We then consider the case of a scatterer placed between two narrow conductors and end up with the Landauer formula. Parts of the presentation follow Datta (1995).

Quantisation of conductance

To determine the current carried by a single electron, we start from the conservation of charge, which can be expressed via the equation of continuity:

$$\partial_t \int \rho d^3x = - \oint \rho \mathbf{v} \cdot d\mathbf{A}. \quad (2.18)$$

This equation must hold for any region in space. With the definition of current density $\mathbf{j} := \rho \mathbf{v}$ and using Gauss' theorem, Eq. (2.18) can be written as

$$\partial_t \rho + \nabla \cdot \mathbf{j} = 0. \quad (2.19)$$

The current dI through an infinitesimal small area $d\mathbf{A}$ is then defined as $dI := \mathbf{j} \cdot d\mathbf{A}$. The current I_e which is produced by a single electron moving with velocity $\mathbf{v}_e = v_e \mathbf{n}$ within a conductor of length L and cross section $\mathbf{A} = A \mathbf{n}$ (\mathbf{n} being the unit normal) therefore is

$$I_e = \frac{-ev_e}{L}. \quad (2.20)$$

Now what is the velocity v_e of an electron? The electronic states within a narrow conductor belong to different bands n . Each of these bands is characterised by its dispersion relation $E_n(\mathbf{k})$. For a narrow conductor along the z -axis, all wave vectors are of the form $\mathbf{k} = k \mathbf{e}_z$. If we take the wave function for an electron with wave vector k_0 to be a Fourier composition of plane waves (all within a single band n) $\psi(x, y, z, t) = \int dk \alpha(n, k) \psi(x, y) \exp(ikz - iE_n(k)t/\hbar)$ with coefficients $\alpha(n, k)$ peaked around k_0 , then the corresponding velocity is given by the group velocity i.e. the velocity of the maximum position of the wave package. The position of the maximum is located at the stationary point of the phase factor:

$$z = \frac{t}{\hbar} \left. \frac{\partial E_n(k)}{\partial k} \right|_{k=k_0} \quad (2.21)$$

and therefore

$$\mathbf{v}_{n, \mathbf{k}_0} = \frac{1}{\hbar} \left. \frac{\partial E_n(\mathbf{k})}{\partial \mathbf{k}} \right|_{\mathbf{k}=\mathbf{k}_0}. \quad (2.22)$$

The total current (in one direction) is produced by all electrons moving in that direction. Assuming the electronic states of the narrow conductor

with $k_z > 0$ to be occupied according to a Fermi function $f(E - \mu_>)$ with chemical potential $\mu_>$, the total current adds up to

$$I^> = -2\frac{e}{L} \sum_{n,k} \frac{1}{\hbar} \frac{\partial E_n(k)}{\partial k} f(E_n(k) - \mu_>). \quad (2.23)$$

The factor of two is included to account for spin degeneracy and the summation runs over all bands n and all $k \in \mathbb{R} : k = 2\pi j/L, j \in \mathbb{N}$. For large L , the sum over k can be approximated by an integral

$$\begin{aligned} I^> &= -\frac{2e}{h} \sum_n \int_0^\infty dk \frac{\partial E_n(k)}{\partial k} f(E_n(k) - \mu_>) \\ &= -\frac{2e}{h} \sum_n \int_{E_n^{\min}}^{E_n^{\max}} dE f(E - \mu_>) \\ &= -\frac{2e}{h} \int_{-\infty}^\infty dE M(E) f(E - \mu_>), \end{aligned} \quad (2.24)$$

where $M(E)$ counts the number of bands with accessible states at energy E .

A few remarks about this result: for a system in equilibrium, where $\mu_< = \mu_>$, the current obtained by Eq. (2.24) is compensated by an equal current in the opposite direction. Only if the two chemical potentials differ, a net current is present. At low temperature and with a relative shift in the chemical potential $\mu_> = \mu_< + eV$ due to a small applied voltage V , the resulting current is

$$I_{\text{tot}} = -M(E_F)G_0V, \quad (2.25)$$

where the quantum of conductance

$$G_0 := \frac{2e^2}{h} \quad (2.26)$$

has been introduced. This is a remarkable result, as each band with accessible states at the Fermi level contributes the same universal amount G_0 to the total conductance $G := dI_{\text{tot}}/dV$.

Current described by transmission – Landauer formula

Now we consider the case where there is a scatterer located in the middle of two narrow conductors as depicted in Fig. 2.1. Within the region to the left of the defect (called region 1), the electrons will produce the incoming current

$$I_1^> = -\frac{2e}{h} \int_{-\infty}^\infty dE M_1(E) f(E - \mu_>) \quad (2.27)$$

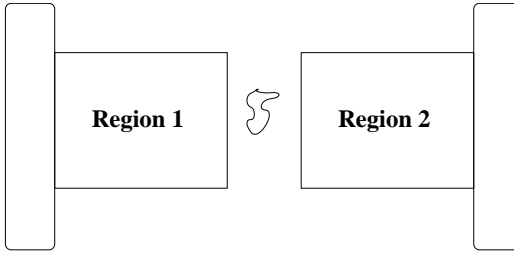


Figure 2.1: Schematic representation of the system. To the left and right there are wide contacts. The defect (in the middle) is coupled to them via small leads with a finite number of modes.

as we have calculated in the previous section (Eq. 2.24). Analogously, the incoming current from region 2 reads

$$I_2^< = -\frac{2e}{h} \int_{-\infty}^{\infty} dE M_2(E) f(E - \mu_<). \quad (2.28)$$

At the defect each incoming wave is scattered in a different way, depending on its energy and the band it belongs to. This scattering redistributes the wave amplitude among all the accessible bands (numbered by $M_1(E)$ in region 1 and $M_2(E)$ in region 2) and results in reflected amplitudes (within conductor 1) and transmitted ones (within conductor 2). We introduce the scattering coefficient $s_{m \leftarrow n}(E', E) := \frac{a_m(E')}{a_n(E)}$, as the ratio of the scattered amplitude $a_m(E')$ within band m at energy E' in region 2 and the incident amplitude $a_n(E)$ within band n at energy E in region 1. These scattering coefficients can either be calculated by Green's function techniques or by directly calculating the scattering matrix (see Sec. 2.2.1 and Sec. 4.2.2).

The current density associated with a wave of amplitude $a_n(E_k)$ is proportional to $|a_n(E_k)|^2 v_n(k)$. This gives rise to the definition of the transmission function $T(E)$:

$$T(E) = \sum_{n \in 1} \sum_{m \in 2} \int T_{m \leftarrow n}(E', E) dE',$$

$$T_{m \leftarrow n}(E', E) = |s_{m \leftarrow n}(E', E)|^2 \frac{v_m}{v_n}.$$

From now on, we will consider elastic scattering only. Therefore the integration over E' can be performed trivially as all transmission coefficients with $E' \neq E$ are zero. And because the scattering matrix is unitary for elastic scattering, the transmission function for transmission from conductor 1 to 2 is identical to the one for transmission from conductor 2 to 1:

$$T(E) = \sum_{n \in 1} \sum_{m \in 2} T_{m \leftarrow n}(E) = \sum_{m \in 2} \sum_{n \in 1} T_{n \leftarrow m}(E). \quad (2.29)$$

Because of charge conservation reflection is described by the function

$$R_i(E) := M_i(E) - T(E), \quad (2.30)$$

where i labels conductor 1 or 2 respectively.

When we replace $M_1(E)$ in Eq. (2.27) by $T(E)$, then we obtain that part of the outgoing current within conductor 2, which is produced by transmission from conductor 1. There is a second part due to reflection of the incoming current of conductor 2, which is obtained by replacing $M_2(E)$ in Eq. (2.28) with $R_2(E)$. The outgoing current in conductor 2 is the sum of both contributions:

$$I_2^> = -\frac{2e}{h} \int [(T(E)f(E - \mu_>) + R_2(E)f(E - \mu_<))] dE. \quad (2.31)$$

The total current within conductor 2 now is the difference between incoming and outgoing currents $I_2^> - I_2^<$:

$$\begin{aligned} I_2^{\text{tot}} &= -\frac{2e}{h} \int [T(E)f(E - \mu_>) + R_2(E)f(E - \mu_<) - M_2(E)f(E - \mu_<)] dE \\ &\stackrel{(2.30)}{=} -\frac{2e}{h} \int T(E)[f(E - \mu_>) - f(E - \mu_<)] dE. \end{aligned} \quad (2.32)$$

This is the so called Landauer formula (Landauer, 1957). Again we see that in equilibrium there will be no net current. Only if the two chemical potentials are biased by an external voltage (see Fig. 2.2), a current can arise across the scatterer.

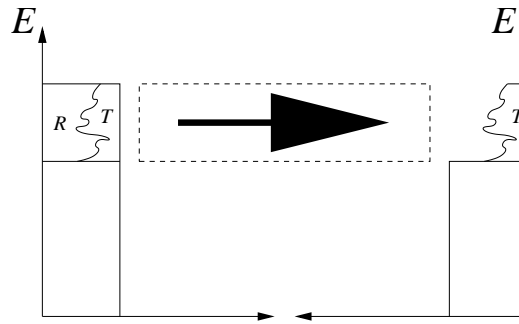


Figure 2.2: The occupation of energy levels within left and right contact at zero temperature. Because of an applied bias there is a net current produced by transmission across the defect.

Chapter 3

Quantum-chemical description of nanoscale systems

Before we describe the basics of quantum-chemical methods for the description of systems on the nanometer scale, we answer the question why we do not use one of the standard models in physics commonly used for small systems, like the Hubbard or Anderson model.

When one deals with an electronic many-particle system, a complete solution starting from first principles is typically not possible. The hardest problem is to treat the electron-electron correlations correctly. In practice, there are two possible approaches to this problem: either one applies approximations with respect to these correlations, or one concentrates on the electronic correlations only, thereby dropping all system dependent information, by discretising the Hilbert space and introducing free parameters describing the interaction between neighbouring electrons. The latter approach provides insight into effects merely produced by interaction and allows for a classification of the underlying model with respect to the parameters. When compared to experimental results, the model parameters can be determined and by this the system under investigation can be classified.

However, it is not always clear how the model parameters have to be adjusted (or if the model is applicable in the first place), when some of the experimentally available parameters are varied. Therefore, the model-Hamiltonian approaches are less suited for studying the influence of experimental details like small variations in the atomic structure or a change in chemical type. For example the scanning tunnelling microscope utilises the high sensitivity of the tunnelling current with respect to tiny changes in the tip position to obtain topographic surface information (see Chap. 6). A theoretical method aiming to reproduce such images has to include the geometrical details of the setup and this is in practice only feasible when approximations to the

treatment of the electron-electron interactions are applied.

Methods which aim to describe systems on the atomic scale are referred to as quantum-chemical. During the years, starting in the late 1920's with the rise of quantum mechanics, a vast number of such methods has been developed. As a first step one distinguishes between ab-initio and semiempirical methods. The first do not take any input parameters besides fundamental physical constants, while the semiempirical methods allow parameters to be either taken from experiment or to be fit to best reproduce experimentally accessible observables. We first consider the ab-initio methods before we turn to the semiempirical ones.

3.1 Ab-initio quantum-chemical methods

As there is quite a number of so called ab-initio methods, it is helpful to characterise them according to the underlying approximations to the many-particle problem. Thereby we are following Zülicke (1985), Szabo and Ostlund (1996) and also Pople (1977).

3.1.1 Separating nuclear and electronic problem

Starting from the non-relativistic Hamiltonian for N electrons and M nuclei

$$H = - \sum_{i=1}^N \frac{\hbar^2}{2m_e} \nabla_i^2 - \sum_{n=1}^M \frac{\hbar^2}{2M_n} \nabla_n^2 - \sum_{i=1}^N \sum_{n=1}^M \frac{e^2 Z_n}{|r_i - R_n|} \\ + \sum_{i=1}^N \sum_{j>i}^N \frac{e^2}{|r_i - r_j|} + \sum_{n=1}^M \sum_{m>n}^M \frac{e^2 Z_n Z_m}{|R_n - R_m|}, \quad (3.1)$$

where M_n is the mass of nucleus n and Z_n is its atomic number, the Born-Oppenheimer or adiabatic approximation (relating back to Born and Oppenheimer, 1927) separates nuclear and electronic degrees of freedom. This is motivated by the different time scales of their motion (see Tab. 3.1) and allows to factorise the total wave function $\Psi^{\text{tot}}(r, R) := \Psi_{\text{nuc}}(R)\Psi_e(r, \sigma, \{R\})$, where $\Psi_{\text{nuc}}(R)$ is the nuclear wave function and $\Psi_e(r, \sigma, \{R\})$ the electronic one, depending explicitly on coordinates r and spin σ of all the N electrons, but where the nuclear positions R enter as fixed parameters only. One then studies the remaining electronic Hamiltonian

$$H_e = - \sum_{i=1}^N \frac{\hbar^2}{2m_e} \nabla_i^2 - \sum_{i=1}^N \sum_{n=1}^M \frac{e^2 Z_n}{|r_i - R_n|} + \sum_{i=1}^N \sum_{j>i}^N \frac{e^2}{|r_i - r_j|} \quad (3.2)$$

	electronic	nuclear
τ_e	$\approx 10^{-15} \dots 10^{-16}$ s	τ_{trans}
		$\approx 10^{-13} \dots 10^{-15}$ s
		E^{trans}
E_e	\approx eV	$\approx 10^{-2} \dots 1$ eV
		E^{vib}
		$\approx 10^{-1} \dots 10^{-2}$ eV
		E^{rot}
		$\approx 10^{-3}$ eV

Table 3.1: Time and energy scales for electronic and nuclear dynamics

for a fixed set of nuclear coordinates $\{R\}$, and separately the nuclear Hamiltonian

$$H_{\text{nuc}} = \sum_{n=1}^M \frac{\hbar^2}{2M_n} \nabla_n^2 + \mathcal{E}_{\text{eff}}, \quad (3.3)$$

where the effective nuclear potential energy $\mathcal{E}_{\text{eff}} := \mathcal{E}_e + \sum_{n=1}^M \sum_{m>n} \frac{e^2 Z_n Z_m}{|R_n - R_m|}$ is the sum of the nuclear potential energy and the electronic energy \mathcal{E}_e obtained from the solution of the Schrödinger equation using the Hamiltonian H_e [Eq. (3.2)]. The Hamiltonian H_{nuc} [Eq. (3.3)] is used in the Schrödinger equation for the nuclear wave function to calculate vibrational, rotational, and translational modes of the nuclei.

In a typical quantum-chemical calculation a structure optimisation is performed as a first step by iteratively solving the Schrödinger equation for the electronic and the nuclear wave functions. As such an iteration is time consuming, the electronic problem is not attacked in full detail. With the resulting coordinates for the atomic positions a detailed calculation of the electronic properties follows, using Eq. (3.2) only, and we restrict ourselves to this latter problem from now on, thereby dropping the electronic subscript e and the nuclear position vector R .

3.1.2 Approximations to the electronic problem

A complete solution to the Schrödinger equation together with the electronic Hamiltonian of Eq. (3.2) results in eigenfunctions and the corresponding eigenenergies. Usually one is interested in ground state properties of the system, which require the calculation of the ground state wave function only. But still, the general problem is of course too hard to be solved exactly, and an approximate ansatz for the form of the wave function $\Psi(r, \sigma)$ has to be made, which includes some special assumptions regarding the dynamical behaviour of the electrons.

In Hartree-Fock theory the Pauli principle is taken into account by using

an anti-symmetrised product of orbital wave functions ϕ :

$$\Psi(r, \sigma) = \frac{1}{\sqrt{N!}} \begin{vmatrix} \phi_1(1) & \cdots & \phi_1(N) \\ \vdots & \ddots & \vdots \\ \phi_N(1) & \cdots & \phi_N(N) \end{vmatrix}, \quad (3.4)$$

where $\phi_i(k)$ abbreviates $\phi_i(r_k \sigma_k)$. This determinant contains the N lowest lying occupied orbitals.

With this ansatz for the wave function, the expectation value for the Hamilton operator can be written as

$$\langle H \rangle_{\text{HF}} = \sum_i h_i + \frac{1}{2} \sum_{ij} J_{ij} - \sum_{ij} \frac{1}{2} K_{ij} \quad (3.5)$$

$$h_i = - \int \phi_i^*(1) \left(\frac{\hbar^2}{2m_e} \nabla^2 + \sum_n \frac{e^2 Z_n}{|r_1 - R_n|} \right) \phi_i(1) d1 \quad (3.6)$$

$$J_{ij} = \int \int \frac{|\phi_i^*(1)|^2 \cdot |\phi_j(2)|^2}{|r_1 - r_2|} d1 d2 \quad (3.7)$$

$$K_{ij} = \int \int \frac{\phi_i^*(1) \phi_j(1) \phi_j^*(2) \phi_i(2)}{|r_1 - r_2|} d1 d2, \quad (3.8)$$

with J the Coulomb integral and K the exchange correlation integral.

Configuration interaction (CI) methods release the restriction to a single determinant wave function. They take sums of determinant wave functions which also include orbitals belonging to excited states. This results in more accurate but also very expensive calculations (Foresman and Frisch, 1996).

For spherically symmetric problems, such as determining the electronic configuration of isolated atoms, the Hartree-Fock method can be used to numerically generate atomic orbital wave functions, which are referred to as *Hartree-Fock atomic orbitals*. The resulting N -particle wave function constitutes the best possible anti-symmetrised product of atomic orbitals for the Hartree-Fock Hamiltonian, i.e. it minimises

$$E = \min_{|\Psi\rangle} \left\{ \frac{\langle H \rangle_{\text{HF}}}{\langle \Psi | \Psi \rangle} \right\}. \quad (3.9)$$

For molecular systems, it is unfortunately out of question to determine the best *molecular* orbital functions (as opposed to the *atomic* orbital functions), because the spherical symmetry is lost (Roothaan, 1951), and thus the Hilbert space of possible functions is just too big. Therefore one additionally has to approximate the molecular orbitals.

3.1.3 Approximations to the molecular orbitals

One possible basis set for molecular orbital wave functions is a set of atomic orbitals. As one then deals with a *linear combination of atomic orbitals*, such a choice is called *LCAO*. Atomic orbitals are of the following form:

$$\begin{aligned}\phi_{nlm}(r, \theta, \phi) &= \sum_j C_{j,nl} \chi_{j,nlm}(r, \theta, \phi) \\ \chi_{nlm} &= R_{nl}(r) Y_{lm}(\theta, \phi) \\ Y_{lm}(\theta, \phi) &= \sqrt{\frac{2l+1}{4\pi} \frac{(l-|m|)!}{(l+|m|)!}} P_l^{|m|}(\cos(\theta)) e^{im\phi}.\end{aligned}\quad (3.10)$$

The Y_{lm} are spherical harmonics and $P_l^m(x)$ denotes the associated Legendre polynomials, the ones corresponding to the $s(l=0)$ and $p(l=1)$ orbitals being:

$$\begin{aligned}P_0^0(x) &= 1, \\ P_1^0(x) &= x, \quad P_1^1(x) = \sqrt{1-x^2}.\end{aligned}$$

Within an LCAO treatment, the exact form of the radial wave function $R_{nl}(r)$ is of great importance and commonly one of the following three choices is being made:

- *Slater type orbitals (STO)*: the radial part of the atomic orbital is taken to have the same asymptotic decay as the hydrogen atomic wave function (Slater, 1930), i.e.

$$R_{nl}(r) = N r^{n-1} e^{-\xi_l r}, \quad (3.11)$$

where $N = \frac{1}{\sqrt{(2n)!}} (2\xi_l)^{n+1/2}$ is a normalisation factor, chosen to let the radial function fulfil $\int r^2 R_{nl} R_{nl} dr = 1$.

- *Gaussian functions*: computationally more efficient than a STO is an exponential decay with a quadratic argument:

$$R_{nl}(r) = N r^{n-1} e^{-\alpha_l r^2}, \quad (3.12)$$

$$N = \left(\frac{2^{n+1} (2\alpha_l)^{n+1/2}}{(2n-1)!! \sqrt{\pi}} \right)^{\frac{1}{2}}. \quad (3.13)$$

Quite often STOs are being expanded into K Gaussian functions of the form (3.12) and then being termed Slater type orbitals at the K -Gaussian level: *STO-KG* (Pople, 1977).

- *Hartree-Fock atomic orbitals:* this choice is a LCAO approach in a strict sense, because these orbitals are optimised for the Hartree-Fock atomic problem. However, they generally result in less accurate values for molecular problems as compared to STOs.

With an atomic orbital basis set chosen, a single molecular orbital ψ is now a linear combination of all the atomic orbitals belonging to all the atoms of the molecule. If the latter are located at the spatial positions R_i , then such a combination assumes the form

$$\psi(\mathbf{r}) = \sum_{i \in \text{atoms}} \sum_{nlm} \alpha_{nlm}^i \phi_{nlm}^i(r - R_i). \quad (3.14)$$

The form of the total molecular wave function again depends on the level of theory. For Hartree-Fock studies it is a single determinant as in Eq. (3.4). The expansion coefficients for the ground state wave function α_{nlm}^i are finally obtained by minimising the total energy according to Eq. (3.9).

3.2 Density functional theory

An approach alternative to the theory of electronic structure outlined above is the so called density functional theory (DFT), ‘in which the electron density distribution $n(r)$, rather than the many-electron wave function’ (Kohn, 1999, p. 1253) is the central quantity that one aims for. Its development began in 1964 and 1965 with the two publications by Hohenberg and Kohn (1964), and by Kohn and Sham (1965) and was recognised by a Nobel Prize in Chemistry in 1998.

From the point of view of the Schrödinger equation, an electronic system is uniquely specified by its external potential V . A complete solution to the associated Hamiltonian

$$H = - \sum_{i=1}^N \frac{\hbar^2}{2m} \nabla_i^2 + \sum_{i=1}^N \sum_{j>i}^N \frac{e^2}{|r_i - r_j|} + V, \quad (3.15)$$

where

$$V = \sum_{i=1}^N V(r_i) \quad (3.16)$$

(together with appropriate boundary conditions) consists of its energy spectrum and the corresponding N -particle eigenfunctions. The latter are in general very complex quantities.

Now DFT is based on the fact (see below) that there exists a one-to-one correspondence between the external potential V and the ground-state electronic density $n(r)$ of the electronic Hamiltonian for that potential. Because many ground-state properties of the system can be obtained directly from this ground-state density, one tries to solve for it.

We will only give a short introduction which is mainly intended to clarify some of the naming conventions associated with the method.

3.2.1 Hohenberg-Kohn formulation of DFT

‘The ground-state density $n(r)$ of a bound system of interacting electrons in some external potential V determines this potential uniquely’ (Kohn, 1999, p. 1259). The proof of this statement is quite simple and goes back to Hohenberg and Kohn (1964).

From the correspondence between ground-state density and external potential it follows that the ground state energy of an interacting electronic system can be obtained by a variational principle, where the variation is with respect to the density $n(r)$, which is a simple function of just one spatial coordinate (Hohenberg and Kohn, 1964):

$$E_0 = \min_{n(r)} \{E_V[n(r)]\}, \quad (3.17)$$

where

$$E_V[n(r)] = \int V(r)n(r)dr + F[n(r)]. \quad (3.18)$$

The latter functional $F[n(r)]$ does not depend on V but contains the kinetic energy of the non-interacting electrons $T[n(r)]$ and a second term specific to the electronic Coulomb interaction, which is not known exactly. The so-called exchange-correlation energy functional $E_{xc}[n(r)]$ is now defined as the difference between the unknown functional F and the kinetic energy functional T together with the Coulomb self-interaction:

$$F[n(r)] = T[n(r)] + \frac{1}{2} \int \frac{n(r)n(r')}{|r - r'|} dr dr' + E_{xc}[n(r)]. \quad (3.19)$$

Writing the density for a given number of N electrons as

$$n(r) = \sum_{i=1}^N |\phi_i(r)|^2, \quad (3.20)$$

where each $\phi_i(r)$ is normalised to unity, the Euler-Lagrange equations to Eq. (3.17) with Eqs. (3.18) and (3.19) take the form of N effective Schrödinger-like equations, which are named after Kohn and Sham (1965):

$$\left(-\frac{\hbar^2}{2m} \nabla^2 + V_{\text{eff}}(r) \right) \phi_i(r) = \epsilon_i \phi_i(r), \quad (3.21)$$

with an effective potential V_{eff} and the exchange correlation potential V_{xc} given as

$$V_{\text{eff}}(r) = V(r) + \int \frac{n(r')}{|r - r'|} dr' + V_{\text{xc}}(r), \quad (3.22)$$

$$V_{\text{xc}}(r) = \frac{\delta}{\delta \tilde{n}(r)} E_{\text{xc}}[\tilde{n}(r)] \Big|_{\tilde{n}(r)=n(r)}. \quad (3.23)$$

The functions ϕ_i constituting the density $n(r)$ are sometimes called Kohn-Sham orbitals. As E_{xc} is now the only functional which remains unknown, one approximates it, most frequently by using the so-called local-density approximation.

3.2.2 Local density approximation

When introducing Eq. (3.21) Kohn and Sham (1965) already came up with a simple approximation for the exchange-correlation energy that is surprisingly useful. Let us denote the exchange-correlation energy density per electron of a uniform electron gas by $\epsilon_{\text{xc}}(n)$. Within the local density approximation, the exchange-correlation energy density of a non-uniform electron distribution $n(r)$ is taken to be a local function $\epsilon_{\text{xc}}(r)$, its value being identical to that of a uniform electron gas with constant charge density $n = n(r)$:

$$\epsilon_{\text{xc}}(r) = \epsilon_{\text{xc}}(n) \Big|_{n=n(r)}. \quad (3.24)$$

Therefore, the explicit form of E_{xc} is

$$E_{\text{xc}}^{\text{LDA}}[n(r)] = \int n(r) \epsilon_{\text{xc}}(n) \Big|_{n=n(r)} d^3r. \quad (3.25)$$

The corresponding LDA exchange-correlation potential reads

$$V_{\text{xc}}^{\text{LDA}}(r) = \epsilon_{\text{xc}}(n) \Big|_{n=n(r)} + \frac{d\epsilon_{\text{xc}}}{dn}. \quad (3.26)$$

Although the approximation appears to be poor, it generally yields very accurate results. A commonly used parameterisation of $\epsilon_{\text{xc}}(n)$ based on Monte-Carlo simulations was given by Perdew and Zunger (1981).

3.2.3 Basis set

With an explicit formula for the exchange-correlation potential, one finally has to choose a basis set for the Kohn-Sham orbitals. Analogously to the Hartree-Fock method, they can be expanded in atomic wave functions. More often one uses a plane waves basis set for the interstitial region between the atoms, while a separate solution of Eq. (3.21) is performed for the core region around each atom. Both types of wave functions then have to be matched at the boundary of the atomic and the interstitial regions. This latter approach is known as the *augmented plane wave* (APW) method.

As the exact form of the wave function within the core region of each atom is more or less irrelevant to the chemically interesting valence orbital region, it is more efficient to replace the exact core potential by approximate *pseudopotentials*. These pseudopotentials are more slowly varying and also much weaker than the core potentials, and allow for an expansion of the wave functions into plane waves only.

With a basis set chosen, the Kohn-Sham equations (3.21) can be solved self consistently, in close analogy to the Hartree-Fock method. Finally, we want to note that the type of basis set resulting in the most accurate solutions strongly depends on the system under consideration. Therefore, a lot of experience is needed if one is interested in quantitative results. This does of course hold for all ab-initio methods for electronic structure calculations.

3.3 Semiempirical methods

In contrast to both of the methods outlined above, which are extremely demanding with respect to computational effort, semiempirical methods have been developed. The name *semiempirical* indicates that these methods have been parameterised to reproduce experimental results. They typically use the same LCAO theory as ab-initio methods. However, many of the more complex integrals are removed or replaced using simple approximations. Empirical parameters and functions are used to compensate for the errors introduced by removing integrals.

We first name the most popular ones and characterise them according to their approximations and then give a detailed outline of one of them, namely the extended-Hückel method, which is the one we have implemented. Beside the references given in the text, a more detailed (but slightly outdated) description can be found in Scholz and Köhler (1981) and Zülicke (1985).

3.3.1 Overview of methods in use

The most famous examples of semiempirical methods are the extended Hückel method (which will be discussed in detail in Sec. 3.3.2) and the molecular orbital (MO) theory. The basic approximations of the latter method which allow to neglect less important integrals of the Hartree-Fock method were developed by Pople et al. in the 1950s and 1960s. A couple of methods arose from this period, the most restrictive being the CNDO-approximation (*Complete Neglect of Differential Overlap*, Pople and Segal, 1966) which completely neglects two-electron interaction integrals. By maintaining the differential overlap between different orbitals for all integrals at a single atomic centre the INDO-approximation is obtained (*Intermediate Neglect of Differential Overlap*, Pople et al., 1967), which improves upon the CNDO-approximation while still considerably reducing the computational effort as compared to ab-initio methods. The least restrictive methods stemming from that era apply the so called NDDO-approximation (*Neglect of Diatomic Differential Overlap*, Pople et al., 1965; Pople and Segal, 1965). Here the differential overlap for orbitals of the same atom in two centre integrals is kept explicitly. Methods applying these approximations are still in use, although usually in modifications intended for interpreting molecular spectra.

More suitable methods for the evaluation of energetic data and also for the prediction of molecular geometries have been developed in the 1970s. The general idea was to not only apply an approximation simple enough for the desired calculation to be feasible but also to upgrade the accuracy of the results by introducing parameters that can be adjusted to fit experimental data. For the MINDO/3-method (*Modified Intermediate Neglect of Differential Overlap/Version 3*, Bingham et al., 1975a,b,c,d) the basic approximations are similar to the INDO-approximation, but the atomic-orbital exponents ξ are treated as free parameters which are being optimised during the course of minimisation. Despite the additional effort to determine these parameters, the accuracy for quantities like the heat of formation and geometry parameters for molecules containing heteroatoms (i.e. non-carbon atoms in organic molecules) is sometimes still quite low. These drawbacks were overcome by the MNDO-method (*Modified Neglect of Differential Overlap*, Dewar and Thiel, 1977). It is based on the NDDO-approximation and additionally improves upon the MINDO/3-method by freezing some of the parameters to values that were optimised using a least-square fit to a set of experimental values known to be otherwise represented poorly. But still, the method fails to reproduce hydrogen bonds and activation energies tend to be too large.

It took several years until a next generation of semiempirical methods

was developed. To avoid terminology confusion with previous semiempirical methods (many of which we have not mentioned), entirely different names were adopted. These are AM1 (*Austin Model 1*, Dewar et al., 1985) and PM3 (*MNDO Parametric Model no. 3*, Stewart, 1989a,b). The new idea was, instead of first identifying and then modifying the faulty approximation which causes the poor results, to rather add a new term with new parameters to the corresponding energy expression and fitting these to experimental values. This approach has proven useful and AM1 or PM3 are nowadays the methods of choice if there is the need for a semiempirical quantum-chemical method capable of producing results that are in quantitative agreement with experiments.

3.3.2 Extended-Hückel method

The Hückel method was originally introduced to treat π -bonding in planar organic molecules (Hückel, 1931a,b, 1932, 1933, 1937a,b). Given a molecule in the xy-plane, the idea was to use a $2p_z$ basis set for each double bonded carbon atom. This treatment has then been extended to non- π electron systems with inclusion of all valence orbitals and is now being called the extended-Hückel method. It was originally developed by Hoffmann (1963).

LCAO ansatz

Making the ansatz that a wave function can be written as a linear combination of atomic orbitals (LCAO), it assumes the general form

$$|\Psi\rangle = \sum_i \sum_l \gamma_l^i |\phi_l^i\rangle, \quad (3.27)$$

where i runs over all atoms (with spatial position R_i) of the system to be described and l labels the orbitals of that atom. Expressed in this basis the one-particle Schrödinger equation reads

$$\sum_{j,k} H_{il,jk} \gamma_k^j = E \sum_{jk} S_{il,jk} \gamma_k^j. \quad (3.28)$$

Here we have introduced the overlap matrix $S_{il,jk} := \langle \phi_l^i | \phi_k^j \rangle$ and the coefficients of the Hamiltonian are $H_{il,jk} := \langle \phi_l^i | H | \phi_k^j \rangle$.

Basis set

For an actual calculation it is necessary to represent the wave function in a well-suited analytic form. There is the obvious requirement that this basis set

should well represent the atomic orbitals, labelled by the principal quantum number n and the orbital quantum number l . But as there is a great number of overlap integrals that have to be calculated, the basis set should also allow a fast calculation of these integrals. Therefore Slater type orbitals (STO) are commonly used, because they have the same asymptotic radial decay as the atomic wave functions (Slater, 1930) and any overlap integral $\langle \phi_i | \phi_j \rangle$ can be reduced to an analytic expression. Their explicit form was already given in Eqs. (3.10) and (3.11). Expansion coefficients $C_{j,nl}, \xi_l$ for various atomic types can be found in the literature. We use parameters optimised for the description of valence orbitals (Hoffmann, 1963; Komiya et al., 1977).

Hamiltonian

The electronic Hamiltonian (3.2) can be split into two parts:

$$H_{\text{single}} = \sum_{n \in \text{atoms}} \sum_{i \in n} \left(-\frac{\hbar^2}{2m_e} \nabla_i^2 - \frac{e^2 Z_n}{|r_i - R_n|} + \sum_{\substack{j \in n \\ j \neq i}} \frac{e^2}{|r_i - r_j|} \right) \quad (3.29)$$

$$\begin{aligned} H_{\text{neglect}} = & \sum_{n \in \text{atoms}} \sum_{i \in n} \left(- \sum_{m \neq n} \frac{e^2 Z_m}{|r_i - R_m|} + \sum_{j \notin n} \frac{e^2}{|r_i - r_j|} \right) \\ & + \sum_{n \in \text{atoms}} \sum_{m > n} \frac{e^2 Z_n Z_m}{|R_n - R_m|}. \end{aligned} \quad (3.30)$$

Here $i \in n$ denotes all electrons i belonging to atom n . The Hamiltonian H_{single} contains intra-atomic contributions only, while all contributions from different atoms are included in H_{neglect} . A one-electron method does account for the energetic contributions contained in H_{single} but neglects the ones corresponding to H_{neglect} . In the extended-Hückel method H_{single} can be represented as a sum of one-electron operators:

$$H_{\text{single}} = \sum_i \alpha_i c_i^\dagger c_i + \sum_i \sum_{j \neq i} \beta_{ij} c_i^\dagger c_j. \quad (3.31)$$

The coefficients α_i and β_{ij} are called *Coulomb integrals* and *resonance integrals*, respectively.

The Coulomb integrals are usually parameterised using ionisation energies taken from experiments and for the resonance integrals a number of formulas have been suggested. For example Wheland (1941) and also Mulliken et al. (1941) took $\beta_{ij} = K \cdot S_{ij}$, whereas the choice $\beta_{ij} = K' \cdot S_{ij}(h_{ii} + h_{jj})$, $K' = 1.75$ goes back to Hoffmann (1962, 1963); Wolfsberg and Helmholtz (1952). We

use the latter one but with a different weighting: $K' = k/2 + a/2 + a^2 \frac{1-k}{2}$, $k = 1.75$, $a = (\frac{h_{ii}-h_{jj}}{h_{ii}+h_{jj}})$.

With a STO basis set the overlap matrix elements

$$S_{ij} = \int d^3x \phi_i \phi_j \quad (3.32)$$

can be reduced to analytic expressions which can be evaluated very efficiently.

Schrödinger equation

For a given molecular structure, described by the positions of all atoms, each atom is equipped with an atomic orbital function for all its valence orbitals. These atomic orbitals are taken as a basis of the Hilbert space. The Hamiltonian matrix elements can then explicitly be calculated in this representation and the Schrödinger equation assumes the matrix form

$$H\gamma = E \cdot S\gamma, \quad (3.33)$$

where the vector γ contains the coefficients of the atomic orbitals. S is the overlap matrix, which takes into account that orbitals at different atoms are non-orthogonal in general. Equation (3.33) constitutes a generalised eigenvalue problem which can be solved using standard methods of linear algebra. Instead of simply inverting S it is however advisable to compute $S^{-1/2}$, which exists uniquely for positive definite overlap matrices. Then Eq. (3.33) can be transformed to

$$S^{-1/2} H S^{-1/2} \gamma' = E \gamma'. \quad (3.34)$$

Thus one obtains an eigenvalue problem for eigenvectors $\gamma' = S^{1/2}\gamma$. Furthermore this eigenvalue problem is symmetric, because S and also H are symmetric matrices.

3.3.3 Concluding remarks

The previous section dealt with the extended-Hückel method, which we have chosen to implement although it is less accurate as compared to AM1 and PM3. The reason for this choice, besides the lesser computational effort, mainly is that we want to perform qualitative studies of considerably large systems. To this end the extended-Hückel method is sufficient. However, it should be noted that there is no restriction to this choice. Any of the methods mentioned in this chapter could also be used, as they all provide an effective single-particle Hamiltonian, which is the only input to the method we use for calculating transport through molecular systems (see Chap. 4).

Chapter 4

The Elastic-Scattering Quantum-Chemistry Method

The original ESQC method ‘offers a means of studying the transmission of electrons through a defect embedded in an infinite, periodic chain’ (Roshd, 1992, p. 8). It was first proposed by Sautet and Joachim (1988a,b,c) who studied the transmission of electrons through a molecular switch. The infinite and periodic chain in these studies was a conducting polymer, while the defect was taken to be a benzene ring. The original, more or less one-dimensional method, was then generalised in such a way that a defect could be embedded in an infinite but periodic three-dimensional wire (Sautet and Joachim, 1991). This improvement allowed for the study of the tunnelling of electrons in a Scanning Tunnelling Microscope (STM), where the defect contains the surface of the substrate together with a molecule adsorbed upon and the apex of the STM tip. The infinite and periodic wire represents the bulk region of tip and substrate. However, in the original presentation the method is restricted to the case that the two bulk regions are identical, which is typically not the case in real STM experiments.

In this chapter, we present a generalised version of ESQC (Dahlke and Schollwöck, 2004), which overcomes the restriction to place the defect between identical leads. Furthermore, it generalises the original setup of two leads to an arbitrary number. These improvements are the result of a thorough treatment of the scattering problem as it is provided here.

4.1 Outline of the ESQC algorithm

The name already suggests that the method is based on the combination of an exact solution to a scattering problem for a Hamiltonian which is obtained

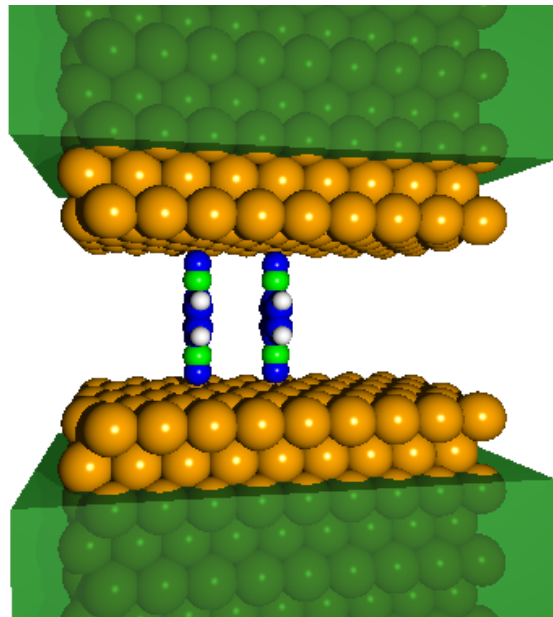


Figure 4.1: Partitioning of the system into individual parts, here for the case of two leads (surrounded by boxes) being attached to the molecular region which also contains the surface atoms of each lead.

from a quantum-chemical calculation. The basic principles of all scattering approaches have already been outlined in Sec. 2.2 while an introduction to quantum-chemical methods is provided in Chap. 3. The present chapter is devoted to an in depth description of the ESQC method and also covers details of the implementation.

The method involves quite a large number of steps to finally obtain the conductance properties of a molecular system. Here we summarise these steps; the calculational details are contained in Sec. 4.2.

4.1.1 Algorithm step by step

As already described in Sec. 2.2 within a scattering approach the solutions to the Schrödinger equation far away from the molecular region are asymptotically equal to solutions of the isolated leads. To obtain these asymptotic states the system is formally divided into several parts, one containing the molecular region and an additional part for each lead. For the case of two leads, this partitioning is sketched in Fig. 4.1.

First the asymptotic states are calculated for each of the leads separately. Then the S -matrix for scattering of the incoming states into the outgoing ones

is calculated. Finally the current is calculated using the Landauer formula. Only the last two steps depend on the geometry of the molecular region.

1. The calculation of the scattering states for each isolated lead contains the following steps which have to be performed only once:

- The periodic lead is split into identical layers.
- The spatial position and chemical nature of each atom within such a layer has to be specified. Then the quantum-chemical calculation is performed for two adjacent layers with appropriate boundary conditions (see below). This results in a layer-independent Hamiltonian.
- With this Hamiltonian one performs a band-structure calculation to determine the Fermi energy.
- For a discrete set of energy values around the Fermi energy an operator describing the current properties is set up and transformed into an eigenmode basis. The corresponding modes represent either incoming or outgoing scattering solutions.

The results for each discrete energy value can now be stored for reusing them in calculations for different molecular setups.

2. The calculation of the scattering matrix involves the following steps:

- Spatial position and chemical nature of each atom within the molecular region enters the quantum-chemical calculation which results in the Hamiltonian for this part.
- The energy dependent scattering matrix is obtained by connecting the modes of each lead to the molecular region. This step is performed for all the above chosen discrete energy values which are within the energy window defined by the chemical potentials of source and drain lead (see Fig. 4.2).

3. Finally the current is calculated in the following way:

- The value of the transmission function for each discrete energy level is obtained by summing up the contribution to the scattering matrix from each channel.
- With the Landauer formula one obtains the current across the molecular region by an integration over these energies.

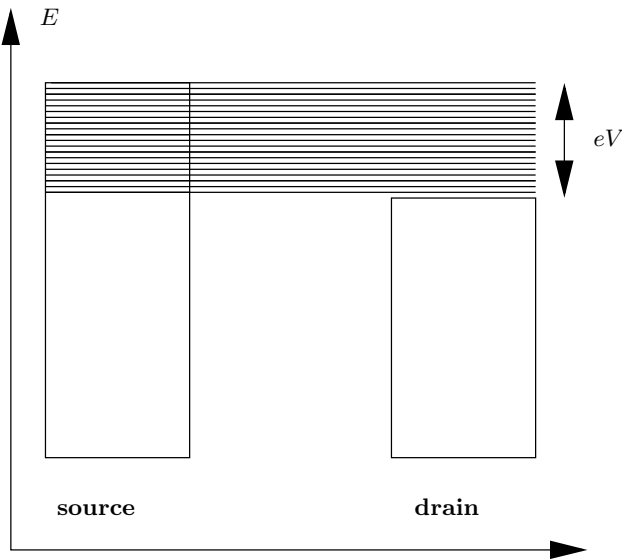


Figure 4.2: Sketch of the set of discrete energy levels between the two chemical potentials of source and drain. At each of these energy levels the scattering matrix has to be calculated. The rectangular boxes represent the zero-temperature Fermi functions of source and drain lead.

It is noted here that the calculations can also be performed using Green's function techniques (see e.g. Datta, 1995) which is equivalent to the scattering matrix approach (as shown by Fisher and Lee, 1981). We present the details of the calculation within the latter framework as then the contributions from individual channels to the transmission function can be studied easily.

Before we go into the details of the steps outlined above we first want to make some remarks about the differences between calculations for STM images and calculations for conductance properties of molecules in molecular electronic devices.

4.1.2 Notes on calculations of conductance properties

To obtain the conductance properties of a molecular electronic device (see Chap. 5), the current across the molecular region has to be calculated for many different applied source-drain voltages. Conductance properties can then be obtained by numerically calculating the derivative of the current with respect to the applied voltage: $G = \frac{dI}{dV}$.

The entire ESQC-algorithm has to be executed for each value of applied

voltage. To gain a proper resolution in voltage space one has to consider quite a large number of discrete energy levels between the chemical potentials of source and drain electrode (see Fig. 4.2). And again for each of these energy levels, step two of the algorithm has to be performed. To increase the accuracy of a conductance calculation one therefore has to increase the number of energy levels and the number of voltage steps. The limiting factor is usually not the computational time but rather the size of available system memory, because a matrix containing the current properties has to be kept in memory for each energy level and each lead.

4.1.3 Notes on STM image calculations

As explained in Chap. 6, an STM image is produced by recording the current or the height of the STM tip while scanning over the sample surface. But the ESQC algorithm results in the current value for a fixed geometry which in the STM context corresponds to a fixed tip position. To obtain an STM image of an entire surface region numerically, one has to model the tip movement. Then, for a finite number of tip positions the current calculation has to be performed.

In order to obtain a reasonable image resolution the current calculation has to be repeated a great many times. But because the calculations for each fixed tip position do not depend on each other this process can efficiently be parallelised.

To keep the computational cost at a reasonable level, it is advisable to take only a few energy levels around the Fermi energy into account. For large molecules adsorbed flat on top of the substrate one even has to restrict to a single such level because due to their size, the Hamiltonian matrices already use up the entire system memory.

4.2 Detailed description of ESQC

As a first step of the ESQC-algorithm the system under consideration has to be decomposed into distinct parts. These parts are described by the same quantum-chemical method but several different calculations have to be performed. The decomposition results in $n+1$ -parts, where n is the number of leads. Let us call them $\Sigma_d, d \in \{0, 1, \dots, n\}$. Σ_0 contains the molecular region and also the top most surface layers of each lead and $\Sigma_d, d > 0$ contains the semi-infinite lead d (see Fig. 4.1 with $n = 2$). Periodic boundary conditions in the directions perpendicular to the surface normal are used.

First we will restrict our attention to the semi-infinite leads, which in

general will be different. In the outline of the ESQC-algorithm as given above this corresponds to step one.

4.2.1 Isolated semi-infinite leads

A microscopic description for each lead is obtained from quantum chemistry, which provides an effective one-particle Hamiltonian. By a tight-binding approximation and using the periodicity of the system, the semi-infinite lead Hamiltonian assumes block tridiagonal form with finite dimensional blocks

$$\begin{aligned} H^d = & \sum_{l=l_0}^{\infty} \sum_{i \in l} \sum_{j < i} \left(H_{lli,j}^d c_{di}^\dagger c_{dlj} + \text{h.c.} \right) \\ & + \sum_{l=l_0}^{\infty} \sum_{i \in l} \sum_{j \in l+1} \left(H_{l,l+1,i,j}^d c_{di}^\dagger c_{d,l+1,j} + \text{h.c.} \right) \end{aligned} \quad (4.1)$$

Layer by layer, starting with the first layer not included in the molecular region (named l_0), the first term accounts for intra-layer interactions, while the second one describes the interaction between layers. The indices i and j run over the orbital basis set within each layer. The size of each layer is chosen such that only adjacent layers have non-zero interaction. It therefore depends on the details of the tight-binding approximation. Figure 4.3 (a) sketches the partitioning of a lead into identical layers.

The Hamiltonian in Eq. (4.1) for one lead d is layer independent, if one assumes periodicity, i.e. $H_{ll}^d = H_{l_0,l_0}^d$ and $H_{l,l+1}^d = H_{l_0,l_0+1}^d$. Therefore, we obtain the following infinite dimensional coupled system of equations:

$$\left(M_d(E) \gamma_l + h_d(E) \gamma_{l+1} + h_d^\dagger(E) \gamma_{l-1} \right) = 0, \quad \forall l \geq l_0 + 1, \quad (4.2)$$

with $M_d(E) := H_{l_0,l_0}^d - E S_{l_0,l_0}^d$, $h_d(E) := H_{l_0,l_0+1}^d - E S_{l_0,l_0+1}^d$, and $S_{ll'}^d$ is the overlap matrix between orbitals in layer l and layer l' of lead d for cases when one does not deal with an orthonormal basis set (otherwise $S_{ll'}^d = \text{Id} \cdot \delta_{ll'}$).

Band-structure calculation

Using Bloch's theorem one can reduce the infinite dimensional system of equations to an $N \times N$ -matrix equation (N being the number of orbital basis functions in one layer)

$$\left(M_d(E) + h_d(E) e^{ik\Delta_d} + h_d^\dagger(E) e^{-ik\Delta_d} \right) \gamma_l(k, E) = 0, \quad \forall l. \quad (4.3)$$

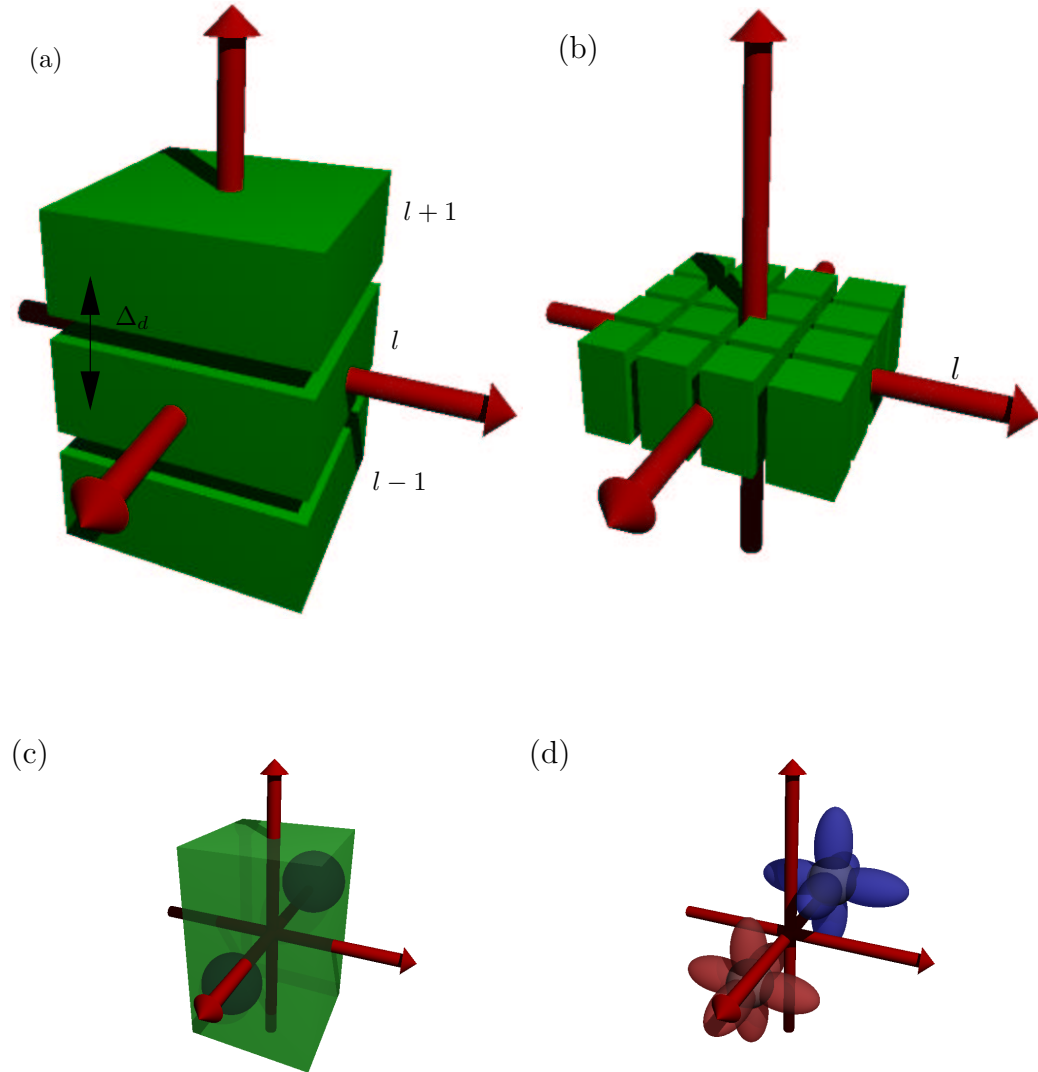


Figure 4.3: (a) Part of the bulk region of a semi-infinite lead which is split into identical layers. (b) Each layer contains identical unit cells and periodic boundary conditions in the lateral direction are applied. (c) Zoom into the unit cell of one layer. The position of the atoms is indicated. (d) Each atom of the unit cell is equipped with a valence orbital basis set.

With Δ_d we denote the (lead dependent) lattice spacing and the layer coefficients γ_l obey the relation $\gamma_{l+1} = e^{ik\Delta_d} \gamma_l$. (From here on we will drop the energy- and k -dependency of γ .)

Fixing the value of k Eq. (4.3) can also be written in the form

$$\tilde{H}\gamma_l = E(k)\tilde{S}\gamma_l, \quad (4.4)$$

which is a generalised eigenvalue problem for $E(k)$ with

$$\begin{aligned}\tilde{H} &:= H_{l_0 l_0}^d + e^{ik\Delta_d} H_{l_0, l_0+1}^d + e^{-ik\Delta_d} H_{l_0+1, l_0}^d \\ \tilde{S} &:= S_{l_0 l_0}^d + e^{ik\Delta_d} S_{l_0, l_0+1}^d + e^{-ik\Delta_d} S_{l_0+1, l_0}^d.\end{aligned}$$

Whenever \tilde{S} is positive definite (which typical overlap matrices happen to be), this equation can be transformed into a normal eigenvalue problem:

$$\begin{aligned}\tilde{S}^{-1/2} \tilde{H} \tilde{S}^{-1/2} x_l &= E(k) x_l, \\ x_l &:= \tilde{S}^{1/2} \gamma_l.\end{aligned} \quad (4.5)$$

Solving for various values of k one obtains the dispersion relation or projected band structure $E(k)$ of the isolated lead. It should be noted here, that for efficiency (and also numerical accuracy) reasons it is advisable to reduce the $N \times N$ dimensional Eq. (4.5) to m different $N_2 \times N_2$ (with $N = m \cdot N_2$) eigenvalue problems by again using Bloch's theorem this time within the lateral direction, i.e. for all m values of $\mathbf{k}_{||}$ which are in accordance with the lateral periodic boundary conditions:

$$\left(\tilde{H}_0 \right)_{ij} = \sum_{c=1}^m e^{i\mathbf{k}_{||} \cdot \mathbf{R}_c} \left(\tilde{H}_c \right)_{ij}. \quad (4.6)$$

Here c runs over all cells within one layer and \mathbf{R}_c denotes the spatial distance to an (arbitrarily chosen) first cell (therefore $\mathbf{R}_1 = 0$). By \tilde{H}_0 we denote the reduced $N_2 \times N_2$ dimensional Hamiltonian, and \tilde{H}_c contains the Hamiltonian elements for orbitals i in the first cell and orbitals j in cell c . An analogous reduction for the overlap matrix results in \tilde{S}_0 . Figure 4.3 (b) sketches the periodicity of a single layer in lateral direction.

With the knowledge of the band structure of a lead, we can determine the Fermi energy by successively filling up the one-particle states starting with the lowest energy state. The conductance properties of the isolated lead are governed by states with energy values at the Fermi level, and these states will be determined next.

Layer-to-layer propagator

To obtain the wave function belonging to a specific energy value E we again turn to Eq. (4.3). Defining $\lambda_d := e^{ik\Delta_d}$ one can easily see that it constitutes an $N \times N$ quadratic eigenvalue problem in λ_d . It can be transformed into a $2N \times 2N$ linear eigenvalue problem:

$$P_d(E) \begin{pmatrix} \gamma_l \\ \gamma_{l+1} \end{pmatrix} = \lambda_d \begin{pmatrix} \gamma_l \\ \gamma_{l+1} \end{pmatrix}, \quad (4.7)$$

$$P_d(E) := \begin{bmatrix} 0 & 1 \\ -h_d^{-1}h_d^\dagger & -h_d^{-1}M_d \end{bmatrix}. \quad (4.8)$$

The eigenvectors of this equation constitute Bloch waves for the semi-infinite lead. We call $P_d(E)$ the layer-to-layer propagator because it also connects the coefficients of adjacent layers

$$\begin{pmatrix} \gamma_l \\ \gamma_{l+1} \end{pmatrix} = P_d(E) \begin{pmatrix} \gamma_{l-1} \\ \gamma_l \end{pmatrix}, \quad (4.9)$$

where we have used Eq. (4.2).

At a given energy E , each eigenvector constitutes an independent channel and the eigenvalue λ_d contains information about its propagation along the lead. The eigenvalues come in pairs such that for each eigenvalue $\lambda_>$, there exists a corresponding eigenvalue $\lambda_<$ satisfying the relation $\lambda_> = 1/\lambda_<^*$, as can be seen by transposing Eq. (4.3). Eigenvalues with $|\lambda| \neq 1$, i.e. complex k , belong to exponentially diverging solutions (see Eq. 4.9 and 4.7). These are of course non physical, as long as the lead is infinite. In semi-infinite leads however (which we are dealing with), exponentially decaying coefficients at the boundary will contribute to the surface wave function and must not be neglected.

Current operator

We have already seen, that the modulus of an eigenvalue reveals information about the propagation properties of the corresponding Bloch wave. However, the contribution to the net current can not directly be seen from Eq. (4.5). It depends on the current density associated with a solution to the Schrödinger equation $i\hbar\partial_t S\gamma = H\gamma$ and is obtained via the continuity equation. The probability amplitude $|\gamma|^2$ for a stationary solution is constant in time

$$\frac{\partial}{\partial t} \gamma^\dagger S\gamma = \frac{i}{\hbar} (\gamma^\dagger H\gamma - \gamma^\dagger H^\dagger \gamma) = 0, \quad (4.10)$$

because H and S are hermitian. For the probability amplitude at all layers between l_1 and l_2 one therefore has

$$\begin{aligned}
0 &= \frac{\partial}{\partial t} \sum_{l=l_1}^{l_2} (\gamma_l^\dagger \gamma_l) \\
&= \frac{i}{\hbar} \sum_{l=l_1}^{l_2} \gamma_l^\dagger (H - H) \gamma_l \\
&= \frac{i}{\hbar} (\gamma_{l_1-1}^\dagger h(E) \gamma_{l_1} + \gamma_{l_1+1}^\dagger h^\dagger(E) \gamma_{l_1} - \text{h.c.}) \\
&\quad + \frac{i}{\hbar} (\gamma_{l_2-1}^\dagger h(E) \gamma_{l_2} + \gamma_{l_2+1}^\dagger h^\dagger(E) \gamma_{l_2} - \text{h.c.}) \\
&= \langle \gamma | l_2, l_2 + 1 \rangle \frac{i}{\hbar} \begin{bmatrix} 0 & -h \\ h^\dagger & 0 \end{bmatrix} \langle l_2, l_2 + 1 | \gamma \rangle \\
&\quad - \langle \gamma | l_1 - 1, l_1 \rangle \frac{i}{\hbar} \begin{bmatrix} 0 & -h \\ h^\dagger & 0 \end{bmatrix} \langle l_1 - 1, l_1 | \gamma \rangle,
\end{aligned} \tag{4.11}$$

with the projectors $\langle l | \gamma \rangle := \gamma_l$. This gives rise to the definition of the current operator W_l for layer l as

$$W_l := |l, l + 1\rangle \frac{i}{\hbar} \begin{bmatrix} 0 & -h \\ h^\dagger & 0 \end{bmatrix} \langle l, l + 1|. \tag{4.12}$$

Now let both φ and ϑ be solutions at fixed energy E with the eigenvalues λ_1 and λ_2 respectively. Because the expectation value for W_l is layer independent (Eq. 4.11) one has:

$$\begin{aligned}
\langle \vartheta | W_l | \varphi \rangle &= \langle \vartheta | W_{l+1} | \varphi \rangle \\
&= \lambda_1 \lambda_2^* \langle \vartheta | W_l | \varphi \rangle.
\end{aligned} \tag{4.13}$$

This equation describes the connection between the current properties of a solution φ and its eigenvalue λ .

Connection between eigenvalues and current properties

The current properties of each channel can be related to the corresponding eigenvalue. We start from Eq. (4.13):

$$\langle \psi | W_j | \phi \rangle = \lambda_1^* \lambda_2 \langle \psi | W_j | \phi \rangle.$$

Let us first consider $|\psi\rangle = |\phi\rangle$, i.e. $\lambda_1 = \lambda_2$, and therefore $\langle \psi | W_j | \phi \rangle = |\lambda| \langle \psi | W_j | \phi \rangle$. For each channel with eigenvalue $|\lambda| \neq 1$ one then must have

$\langle \psi | W_j | \psi \rangle = 0$, i.e. this channel does not carry any current itself. This is consistent with our terminology of an evanescent wave. If, however, $|\lambda_i| = 1$, then $\langle \psi | W_j | \psi \rangle$ is purely imaginary, because W_j is an anti-hermitian operator. We can therefore define the velocity of a propagating wave to be $v_i := \text{Im} \langle \psi | W_j | \psi \rangle$.

Now we consider the case of two different solutions $|\psi\rangle \neq |\phi\rangle$ and define $v_{1,2} := \langle \psi | W_j | \phi \rangle$. If their eigenvalues do not satisfy $\lambda_1 \lambda_2^* = 1$, then the current between these two solutions is zero $v_{1,2} = 0$. So let us assume $\lambda_1 = 1/\lambda_2^*$. Because if $|\lambda_1| > 1$ then $|\lambda_2| < 1$, a current can flow between an evanescent left going wave and an evanescent right going wave. But if we restrict ourselves to solutions with finite amplitudes in a semi-infinite lead, then either the left or right going wave amplitude must be zero. Therefore, evanescent waves do neither carry a current themselves nor do they exchange current with other channels, that is they do not at all contribute to the net current.

Finally, we are left with the case $\lambda_1 = 1/\lambda_2^*$, with $|\lambda_1| = |\lambda_2| = 1$. This is equivalent to $\lambda_1 = \lambda_2$, i.e. the case of degenerate eigenvalues. Therefore propagating waves to degenerate eigenvalues do exchange current. That in turn means that the current of a superposition of two such waves does not necessarily equal the sum of the two individual currents, which is problematic as we want to express the total current as a sum of independent channels. However, the propagating and evanescent waves were obtained by diagonalising the propagator P . This transformation is unique up to rotations in every degenerate eigenvalue subspace. Because W is anti-hermitian we can diagonalise these subspaces and the resulting diagonal elements will be purely imaginary. So the net current may be written as a summation over all the individual contributions of propagating channels, only if these subspace rotations are performed.

Summarising, we have shown that the transformation U diagonalising the propagator P (i.e $U^{-1}PU$) can be chosen in such a way that the transformation $U^\dagger W U$ of the current operator is diagonal in the subspace of propagating waves with purely imaginary diagonal elements. All the other diagonal entries are zero and the only non-zero non-diagonal elements belong to evanescent waves in opposite directions. The relations between eigenvalue, current value and propagation properties are summarised in Table 4.1.

Solutions for an isolated lead are linear combinations of propagating waves in opposite directions, with the same amount of current being transported in each direction, thus carrying no net current, and resulting in a standing wave.

We now define $\Lambda_>$ and $\Lambda_<$ as the two $N \times N$ diagonal matrices composed of all incoming and outgoing eigenvalues $\Lambda_{\geqslant} := \text{diag}(\lambda_{\geqslant}^i)$. The $2N \times 2N$ -

$ \lambda $	v	description		
> 1	0	evanescent	right	going wave
< 1			left	
$\equiv 1$	> 0	propagating	right	going wave
	< 0		left	

Table 4.1: Summary of the connection between eigenvalue, current value and propagation properties

matrix U , which diagonalises P :

$$U^{-1}PU = \begin{bmatrix} \Lambda_> & 0 \\ 0 & \Lambda_< \end{bmatrix}, \quad (4.14)$$

has the following quadratic block form:

$$\begin{bmatrix} U_> & U_< \\ U_>\Lambda_> & U_<\Lambda_< \end{bmatrix}. \quad (4.15)$$

After this transformation into the diagonal basis of the propagator, we can easily obtain all physically relevant solutions of the infinite lead by specifying the amplitudes of all propagating waves at one lattice site.

Now that we have obtained a complete description of the transport properties for all leads, we can turn our attention to the molecular region.

4.2.2 Connecting leads via a molecular region

Up to now, we have considered the isolated leads only. These are now assumed to be each coupled to the molecular defect region and thereby indirectly coupled to one another. We will use the same quantum-chemical description for all three regions, the lead itself, the contact region, and the molecular region. The Hamiltonian for the lead itself has already been set up (Eq. 4.3). Thus, there are still two parts to be determined:

$$H^{\text{mol}} = \sum_{i \in \text{mol}} (\varepsilon_i c_{mi}^\dagger c_{mi} + \sum_{j \neq i} H_{ij}^m c_{mi}^\dagger c_{mj}) \quad (4.16)$$

$$H^{\text{contact}} = \sum_{d \in \text{leads}} \sum_{i \in l_0} \sum_{j \in \text{mol}} (H_{l_0 ij}^{dm} c_{dl_0 i}^\dagger c_{mj} + \text{h.c.}) \quad (4.17)$$

The first Hamiltonian H^{mol} describes the molecular region in absence of the leads, while H^{contact} describes the interaction between the top-most layers

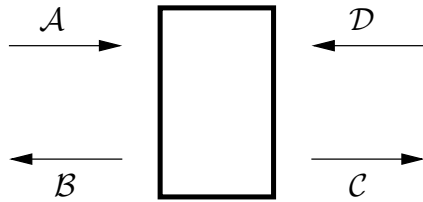


Figure 4.4: Incoming and outgoing wave amplitudes

of each lead and the molecular region. Both Hamiltonians together with the diagonalised layer-to-layer propagators for each lead will now be used to calculate the transmission function.

Scattering matrix

We are interested in stationary solutions, which consist of an incoming propagating wave in one lead, being scattered among all the accessible outgoing channels (propagating and evanescent ones). This information is contained in the scattering matrix \mathcal{S}

$$\begin{pmatrix} \mathcal{B} \\ \mathcal{C} \end{pmatrix} = \underbrace{\begin{bmatrix} \mathcal{S}_{11} & \mathcal{S}_{12} \\ \mathcal{S}_{21} & \mathcal{S}_{22} \end{bmatrix}}_{=: \mathcal{S}} \begin{pmatrix} \mathcal{A} \\ \mathcal{D} \end{pmatrix}, \quad (4.18)$$

which determines the wave amplitudes of all outgoing waves \mathcal{B}, \mathcal{C} given the incoming ones \mathcal{A}, \mathcal{D} .

It is important to notice that the scattering matrix is always quadratic, because in each lead there are the same amount of incoming and outgoing channels. This is opposed to the transfer matrix \mathcal{T} , which connects the amplitudes of in- and outgoing waves \mathcal{C}, \mathcal{D} in one lead to the in- and outgoing waves \mathcal{A}, \mathcal{B} of a second lead:

$$\begin{pmatrix} \mathcal{C} \\ \mathcal{D} \end{pmatrix} = \mathcal{T} \begin{pmatrix} \mathcal{A} \\ \mathcal{B} \end{pmatrix}. \quad (4.19)$$

This matrix is quadratic only if both leads have the same number of channels. It is then of the form (see Roshd, 1992)

$$\mathcal{T} = \begin{bmatrix} F & G^\dagger \\ G & F^\dagger \end{bmatrix} \quad (4.20)$$

and the relation to the scattering matrix is (Roshd, 1992)

$$\mathcal{S} = \begin{bmatrix} -F^{\dagger(-1)}G & F^{\dagger(-1)} \\ F^{-1} & G^\dagger F^{\dagger(-1)} \end{bmatrix}. \quad (4.21)$$

Methods calculating the scattering matrix via the transfer matrix (based on the work of Sautet and Joachim, 1988b) fail, if two types of leads are used, because F then is no longer quadratic and can not be inverted. Therefore, one commonly takes source and drain lead to be identically constituted. But even in such cases, the method becomes numerically unstable, with increasing distance between the molecular region and one lead, because the matrix elements of F and G (in Eq. 4.20) diverge exponentially, with increasing lead separation. Taking the inverse of F is therefore a numerically critical procedure. Both these problems are avoided by the direct calculation of the scattering matrix, which we will now present. This calculation is well defined without any restrictions to the number of leads and their composition. That means that it is not necessary to restrict to identical leads. Furthermore, it allows a numerically stable determination of the scattering matrix, even for weak coupling.

The part of the Hamiltonian containing the molecular region and its coupling to the leads can be written as

$$(H - ES)|\psi\rangle = \begin{bmatrix} h_1 & M_1 & 0 & 0 & \tau_1^\dagger \\ 0 & 0 & h_2 & M_2 & \tau_2^\dagger \\ 0 & \tau_1 & 0 & \tau_2 & M_0 \end{bmatrix} |\psi\rangle = 0. \quad (4.22)$$

(Using this order for the coefficients it is straight forward to extend all formulas to the general case of more than two leads.) The indices 1 and 2 indicate source and drain lead surface layers, while the index 0 is used for the molecular region. $\tau_{1,2}$ are the coupling matrices from source/drain to the molecules.

We now transform each lead into the basis of incoming and outgoing channels (Eq. 4.14), i.e. we apply

$$U = \begin{bmatrix} U^1 & 0 & 0 \\ 0 & U^2 & 0 \\ 0 & 0 & 1 \end{bmatrix},$$

with

$$U^i = \begin{bmatrix} U_>^i & U_<^i \\ U_>^i \Lambda_>^i & U_<^i \Lambda_<^i \end{bmatrix}$$

from the right to Eq. (4.22):

$$(H - ES)U = \begin{bmatrix} A_>^1 & A_<^1 & 0 & 0 & \tau_1^\dagger \\ 0 & 0 & A_>^2 & A_<^2 & \tau_2^\dagger \\ B_>^1 & B_<^1 & B_>^2 & B_<^2 & M_0 \end{bmatrix}, \quad (4.23)$$

with

$$A_{\gtrless}^i = h_i U_{\gtrless}^i + M_i U_{\gtrless}^i \Lambda_{\gtrless}^i,$$

and

$$B_{\gtrless}^i = \tau_i U_{\gtrless}^i \Lambda_{\gtrless}^i.$$

The first and third column act on the surface layer of the incoming channels, the second and fourth act on outgoing ones, while the fifth column, acting on the molecular region, remains unchanged.

The scattering matrix expresses the outgoing channel amplitudes in terms of the incoming ones. Therefore, we split the matrix of Eq. (4.23) into two parts, one containing the outgoing columns, the other one containing the incoming ones as well as the molecular column:

$$M_{\text{out}} := \begin{bmatrix} A_{<}^1 & 0 & \tau_1^\dagger \\ 0 & A_{<}^2 & \tau_2^\dagger \\ B_{<}^1 & B_{<}^2 & M_0 \end{bmatrix}, \quad M_{\text{in}} := \begin{bmatrix} A_{>}^1 & 0 \\ 0 & A_{>}^2 \\ B_{>}^1 & B_{>}^2 \end{bmatrix}.$$

The first matrix M_{out} is a square matrix and by inverting it, we obtain the scattering matrix

$$\mathcal{S} = -M_{\text{out}}^{-1} \cdot M_{\text{in}}. \quad (4.24)$$

4.2.3 Numerical implementation

Let us conclude this chapter with remarks about numerical efficiency. Within the innermost loop of the algorithm for calculating the transmission function, one has to calculate the scattering matrix. This is therefore the right place for optimisation. The \mathcal{S} -matrix as given in Eq. (4.24) is of the form $X = A^{-1} \cdot B$ and citing the Numerical Recipes one ‘should LU decompose A and then back-substitute with the columns of B instead of with the unit vectors that would give A ’s inverse. This saves a whole matrix multiplication, and is also more accurate’ (Press et al., 1999, p. 49). Thus we restate the problem as

$$A \cdot X = B, \quad (4.25)$$

which we have to solve for X .

Now it should be noted that for calculating the transmission probability we do not need the full scattering matrix (now called X), but only those column vectors, which correspond to incoming propagating waves from the source lead. Say that we have d_1 orbitals in each layer of the source lead and d_2 in the drain lead. Then we have $d_1 + d_2$ incoming channels. The number of *propagating* incoming channels p_1 is always significantly smaller.

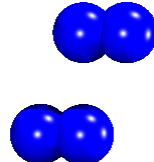


Figure 4.5: The bulk graphite unit cell for one layer contains two atoms. Two layers are needed to generate a periodic super layer. Therefore, the super-layer unit cell contains four atoms.

And therefore, we do not need to substitute back all the $d_1 + d_2$ column vectors of B , but only a small fraction, namely $p_1 \ll d_1$.

Let us consider an example: the primitive cell of graphite contains two atoms, and two primitive layers are needed to build up a periodic super layer (see Fig. 4.5). Each of the carbon atoms is equipped with one 2s and three 2p valence orbitals, i.e. the super-layer unit cell contains 16 orbitals. For a 7×7 super layer of graphite (see Figs. 4.6 and 4.7) the total number of orbitals amounts to $d_1 = 7 \cdot 7 \cdot 16 = 784$. However, the number of propagating channels is only of the order of ten: $p_1 \approx 10$ (the exact value depends on the energy).

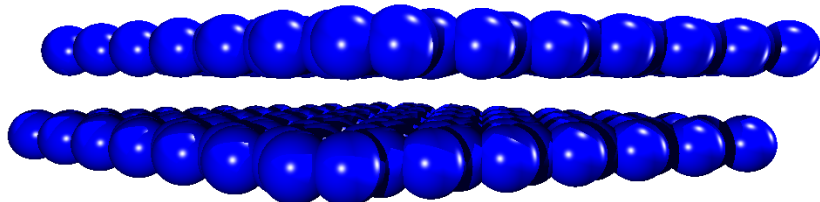


Figure 4.6: When the unit cell is expanded to a 7×7 super cell two graphite layers are generated shown in side view.

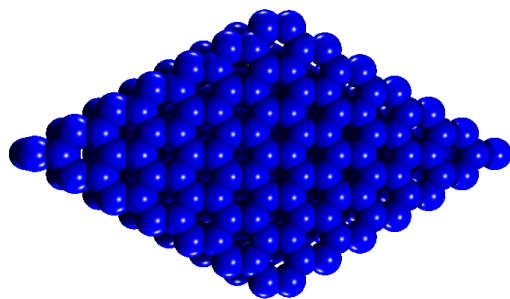


Figure 4.7: Top view of the 7×7 super cell containing 196 atoms.

Chapter 5

Using molecules as electronic devices

Within the last decade an increasing interest in molecular electronics has developed, with the expectation of realising molecular diodes and transistors. This is based on the progress in manipulation techniques, which now allow the controlled attachment of atomic scale structures like molecules to mesoscopic leads. With these new devices one is able to determine the conductance properties of molecular structures. Explaining and predicting the electronic behaviour of such devices is an essential step towards their design and use as nanoscale electronic circuits.

This chapter starts with an historical overview, followed by a qualitative explanation of the occurrence of conductance peaks in molecular electronic devices. We then briefly review some recent experiments and finally turn to our own numerical studies. We analyse possible answers to a question raised in a recent experiment, using the elastic-scattering quantum-chemistry method and give a detailed discussion of our findings (which are published in Dahlke and Schollwöck, 2004).

5.1 Historical overview

5.1.1 Theoretical prediction

The idea of using molecules as building blocks for electronic devices relates back to the year 1974, when Aviram and Ratner suggested the ‘construction of a very simple electronic device, a rectifier, based on the use of a single organic molecule’ (Aviram and Ratner, 1974, p. 277). Because common solid-state rectifiers are based on p–n junctions they argued that an organic

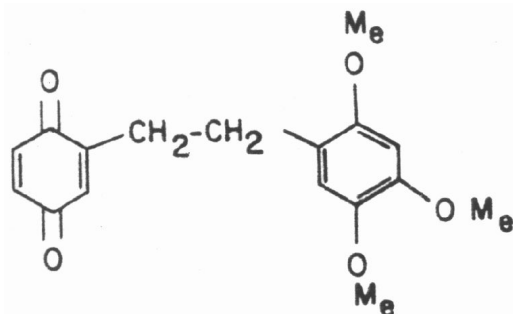


Figure 5.1: An example for a molecule which may act as a rectifier suggested by (and taken from) Aviram and Ratner (1974). M_e s on the right hand side represent methoxy groups ($-\text{OCH}_3$) which constitute the donor region. The quino groups ($=\text{O}$) on the left hand side provide the acceptor state while the methylene bridge ($-\text{CH}_2-$) ensures insulation.

molecule, to show the properties of a rectifier, should consist of an electron-poor subunit on one side (acceptor) and an electron-rich subunit on the opposite side (donor). These subunits have to be effectively insulated from one another to prevent a donor electron from occupying and thereby blocking the acceptor state. As an example, they imagined a certain hemiquinone molecule (shown in Fig. 5.1) to fulfil these requirements.

The energy versus distance diagram for a rectifying molecule is sketched in Fig. 5.2. The acceptor state B on the left hand side of the molecule is required to lie at or slightly above the Fermi level. The donor state C on the right hand side has to lie below both the Fermi level and the acceptor state B .

The energy diagram for the conducting direction is sketched in Fig. 5.3. As soon as an applied voltage becomes large enough for the source levels to overlap with the acceptor level B of the molecule, electron transfer onto the molecule becomes possible. A similar situation on the opposite side enables transfer from the donor level C to the drain lead. Finally, electron transfer from the (now occupied) acceptor state B to the ionised donor state C consists of a two step process: elastic tunnelling from state B to a vibrationally excited Franck-Condon state of C is followed by a decay into the unexcited state C .

With reverse-biasing the asymmetric energy offset of acceptor and donor side prevents the above electron transfer process unless the Fermi level of the source lead (now on the right hand side) is raised to level D (see Fig. 5.4). However, there is a second transfer process which consists of elastic tunnelling from C to B and subsequent tunnelling from B into the drain

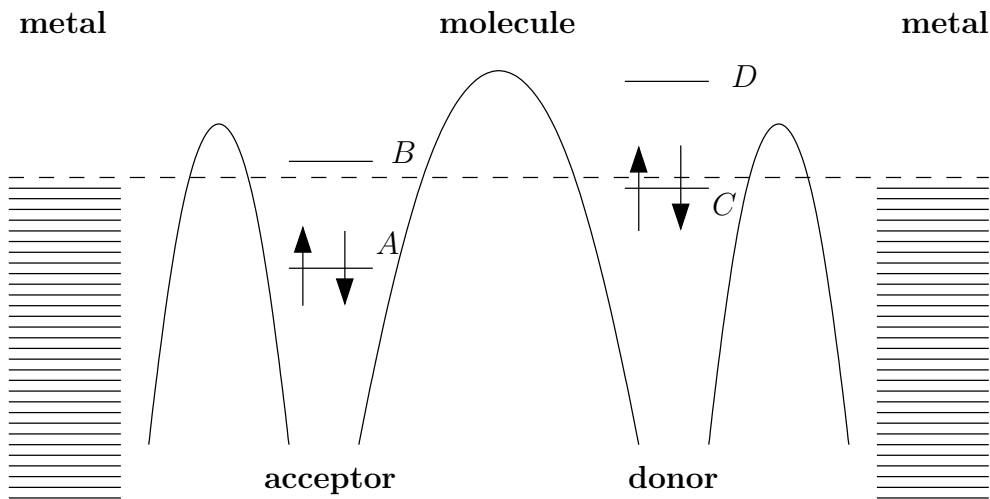


Figure 5.2: Schematic energy versus distance diagram for a molecular rectifier as suggested by Aviram and Ratner (1974). No bias voltage is applied. The unoccupied molecular level on the left hand side is lower lying compared to the one on the right hand side and therefore represents an electron acceptor state. The state on the right hand side represents a donor state.

lead. The voltage threshold for this latter process is governed by the energy difference between states B and C because elastic tunnelling can only occur when level B has been lowered in energy to be in resonance with level C .

When the threshold value involved for tunnelling in the forward direction is smaller than the one for tunnelling in the opposite direction, then the molecule acts as a rectifier. These threshold values do of course depend on the details of the coupling between molecule and both leads as well as the electronic structure of the molecule itself.

5.1.2 Experimental realisation

Because the molecule suggested by Aviram and Ratner (1974) does not couple to metallic leads sufficiently strong, it was never used in experiments aiming to measure the conductance properties of molecules. It took more than 20 years before one of the first experimental realisations succeeded. Geddes et al. (1990) were able to resolve a rectification effect in molecular films on top of platinum surfaces. Later Metzger et al. (1997) were able to address fewer molecules. They reported that ‘current-voltage measurements reveal asymmetries in the DC electrical conductivity through Langmuir-Blodgett multilayers and even monolayers of γ -(*n*-hexadecyl)quinolinium tricyanoquinodimethanide, $C_{16}H_{33}Q - 3CNQ$ ’ (Metzger et al., 1997, p. 10455).

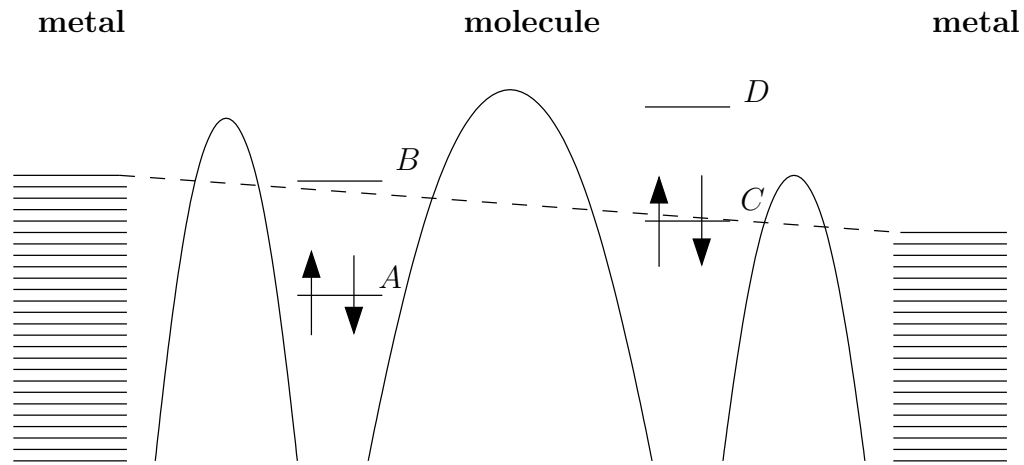


Figure 5.3: Shift of energy levels due to an applied bias in forward direction.

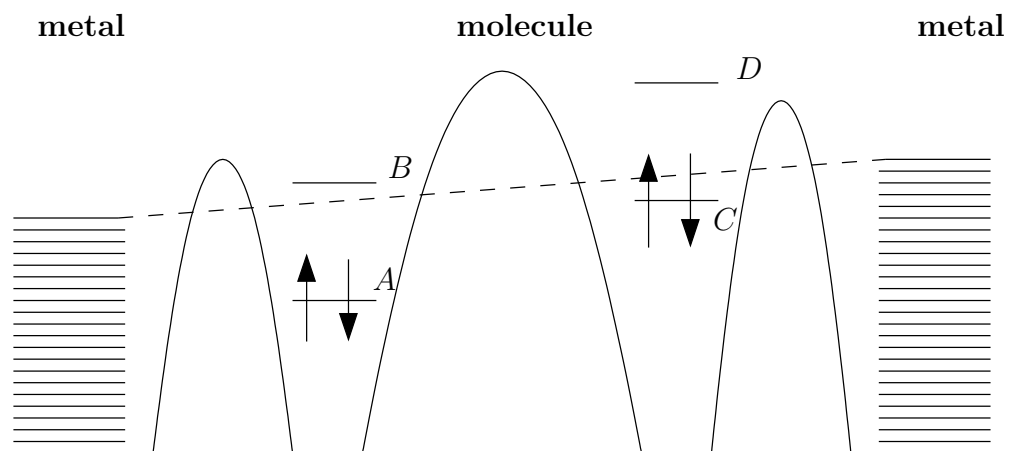


Figure 5.4: Shift of energy levels under reverse bias.

Measurements with a single conducting molecule were first reported by Reed et al. (1997), and since then a lot of experiments using single or few molecules have been performed by various groups. Despite this experimental success, a detailed understanding of the connection between the molecular setup of a device and its conduction properties is still lacking, and a lot of fundamental questions have not yet been answered. First of all, the experimental results seem to be extremely sensitive to the fabrication process. Unfortunately the detailed structure of the molecular region is unknown, because it is experimentally not observable. Therefore, numerical studies have to assume a certain geometrical structure. However, all calculations tend to overestimate the observed magnitude of the current by up to one or two orders of magnitude.

5.2 Qualitative model for transport

The model picture which was introduced by Aviram and Ratner to predict a molecular rectifier (Sec. 5.1.1) views the molecule as consisting of two spatially separated islands, each providing two relevant electronic levels. This picture was motivated by an analogy to semiconductor p-n junctions where one deals with structures on the scale of micrometers.

Although molecular-electronic levels do indeed correspond to separated molecular orbitals, their spatial distance is on the atomic scale, i.e. of the order of Ångstrøms. Furthermore, both leads are only a few nanometers apart. In other words, the entire molecular junction is on the scale of (if not below) the interface region of standard semiconductor devices. The idea of spatially separated energy levels, which are stable under perturbations such as a strong coupling to the leads, the transfer of charge, or an applied bias voltage, is therefore at least questionable.

Because the coupling between molecule and lead surface is produced by a chemical bond it will necessarily be strong. This invalidates the idea of a separate island (let alone two islands) sitting between the contacts, as the lifetime of an additional charge on the molecule scales inversely with the coupling to the leads. We rather think of the molecular region as inducing a modification of the potential gap between both leads. The molecular levels, shifted and broadened by the coupling to the leads, then allow for resonant tunnelling across the barrier region. The spatial location of the molecular orbitals does not provide a stable island, but it does influence the strength of the coupling to the left and the right lead and this results in different couplings to each of them.

5.3 Recent experiments

As the experiments that measure conductance properties of molecular structures vary not only in amount and chemical structure of the molecules in use but also in the way these are attached to metallic or semiconducting leads, we want to give a short overview of the different setups in use. There are basically three different types of devices in use: single or few molecules are accessible in mechanically controllable break junction (MCB) experiments and with the scanning tunnelling microscope (STM), while many molecules are involved in sandwiched self-assembled monolayer (SAM) experiments.

For an explanation of the working principle of the STM we refer to Chap. 6. MCB's are produced by mechanically breaking a lithographically manufactured small bridge connecting two leads. The spatial gap between both leads is then tunable by piezo-electric techniques. When specific molecules are deposited onto the device, a small fraction will be adsorbed in the gap region and there is the chance that a few of them even bridge the gap. By applying a tunable voltage between both the leads, conductance properties of this molecular-electronic device can be measured.

Self-assembled monolayer devices are manufactured in a three step procedure. First a single lead (typically having the form of a finger) is lithographically produced. Then a solution containing the molecules which are known to self-assemble on top of the lead surface is spilt over the device, and within the time scale of hours a monolayer is built. In the final step, a second lead is created on top of the molecular monolayer by beam epitaxy. Again conductance properties of the resulting device can be measured by biasing the leads with an external voltage.

The observed properties depend not only on the molecular species bridging the contacts but also on the exact geometry of the entire device. The conductance measured with different setups can differ in orders of magnitude and the qualitative voltage dependencies of the current ranges from simple ohmic behaviour to asymmetric behaviour and negative differential resistance (NDR).

Reed et al. (1997) have measured the conductance of a self-assembled molecular monolayer bridging an MCB at room temperature, using molecules of 1,4-benzene dithiol (i.e. having two thiol groups as can be seen in Fig. 5.5, which are known to couple strongly to Au-atoms). The conductance-voltage (CV) characteristic was found to be symmetric with one peak in the voltage range of 0–2V. They measured a current of the order of 50nA at a bias voltage of 2V, which they claim is produced by transport through one single active molecule. Reichert et al. (2002) also used an MCB with molecules having two thiol groups, but being considerably longer. The measured current amplitude

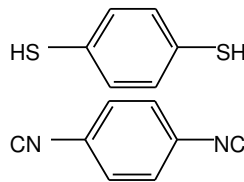


Figure 5.5: Chemical structure of 1,4-benzene dithiol (top) and 1,4-phenylene diisocyanide (bottom).

was about 500nA at 1V for a single molecule, i.e. although the molecule was more than twice as long, the current was ten times larger.

With a different setup with an SAM sandwiched between two metallic leads Chen et al. (1999) have found negative differential resistance, namely one peak at 2V in the *IV* curve. The molecule under investigation had one thiol group only and was attached to Au-leads at both ends. The measurements were taken at room temperature, and the measured current maximum was of the order of 1nA.

Only recently, sandwiched SAM devices were studied at 4.2K (Lee et al., 2003; Dupraz et al., 2003), where 1,4-phenylene diisocyanide (PDI), a benzene ring with two isocyanide instead of thiol groups was used (see Fig. 5.5). The measurements exhibited currents of the order of 50 – 400nA. The *CV* characteristic for this molecule revealed more structure, in form of three to five peaks within a voltage range of 1V. Such a behaviour was not observed with previous devices containing other molecules.

In the next section we want to address the question whether the occurrence of a large amount of conductance peaks within the SAM experiments is contrary to the interpretation of such peaks being produced by resonant tunnelling of electrons through individual molecular orbitals. Before doing so we first give an overview of other numerical studies which have been performed recently.

5.4 Numerical calculations

Aiming to explain the various experimentally observed features of molecular-electronic devices, a number of theoretical methods have been invoked. As one deals with a complex system, quite a number of effects are believed to influence the conductance properties. For example the external bias voltage, an induced electric field, and equilibrium charge transfer between molecule and surface are believed to play an important role to name some of the effects. It has proven fruitful to analyse the influence of a single effect isolated from

the others.

5.4.1 Short summary of recent theoretical studies

Ab-initio calculations for the system studied experimentally by Reed et al. (1997) (see Sec. 5.3) were presented by DiVentra et al. (2000). Using a jellium model representing the gold leads, they were able to reproduce the current-voltage characteristics qualitatively. However, the absolute magnitude of the calculated current was about 2 orders of magnitude larger than the experimental values. Although they were able to reduce the current value significantly by introducing a single gold atom between lead surface and molecule, the final current was still systematically too large. This indicates that numerical calculations need to take the atomic structure of the lead surface into account properly, in order to represent the geometry of the device accurately. The overestimation of the absolute magnitude of the current by most of the theoretical methods, is still an open problem (Emberly and Kirczenow, 2001; Bauschlicher et al., 2003). A solution will also have to explain the origin of the fairly large range of experimentally observed current values (see Sec. 5.3).

Static charge transfer from the metal surface to the molecule was investigated by Xue et al. (2001). They found that such a charge transfer is present and takes influence in that the molecular levels get shifted towards the Fermi energy compared to the position of the isolated molecule. This indicates that static charge transfer processes have to be accounted for, whenever a quantitative calculation of energy levels is aspired.

Along with an applied bias there will also be an electrostatic field across the gap region. To be able to account for this external field, a self consistent procedure together with a solution of the electrostatic problem was applied by Brandbyge et al. (2002). Their results were in agreement with previous calculations neglecting these effects. This indicates that approaches which are less sophisticated with respect to the electrostatic field should be sufficient.

Another interesting question is how the molecular orbital structure takes influence on the conductance properties. This has been studied by Seminario et al. (2001); Darosa and Seminario (2001); Piccini et al. (2003). The aim is to relate different kinds of molecular orbital structures to certain conductance features, which may allow one day to engineer molecules with predefined conductance properties systematically.

The occurrence of negative differential conductance (NDC) has been studied by Hettler et al. (2002, 2003). As already mentioned in Chapter 2 they use a rate equation based approach which is valid for weak coupling only. They argued that transitions between molecular levels around the Fermi en-

ergy can be forbidden due to different symmetry properties. This can result in an isolated level which, if once occupied (via a photon assisted process) ends up blocking further transport. Negative differential conductance is then caused by this blocking.

After this overview of the questions which have been investigated so far, we now consider a problem that occurred when interpreting the findings of a recent experiment. This is the subject of the next section.

5.4.2 Conduction properties of PDI devices

Low temperature experiments with 1,4-phenylene diisocyanide (PDI) SAM's sandwiched between two metallic leads have been performed by Lee et al. (2003) and Dupraz et al. (2003). They show several peaks in the *CV*-diagram. The typical voltage differences of these peaks are in the range of $\Delta U \approx 0.2\text{V}$ (i.e. there are about 5 peaks within $U = 0\text{V}$ and $U = 1\text{V}$). The commonly adopted explanation for the occurrence of such peaks is the following. Each molecular orbital that enters the energy window, which is opened by the applied voltage, enables resonant tunnelling. This increases the conductance and therefore results in a peak within the *CV*-diagram.

Typically, the energy gap between molecular orbitals is in the range of $\Delta E \approx 1\text{eV}$. In other words, for applied voltages up to $U = 1\text{V}$ there should be only a single accessible orbital per molecule, giving rise to only a single peak in the *CV*-diagram (assuming identical contributions from each molecule, which is motivated below). Therefore the following question arises: are there geometrical alignments of the molecules which allow the additional peaks in the *CV* diagram to be explained by resonant tunnelling through molecular orbitals as well?

Influence of changes in the molecular alignment to the transmission spectrum

During the device fabrication, the step under least experimental control is the adsorption of the molecules onto the leads. Therefore the exact geometrical alignment of the molecular SAM is not exactly known. Furthermore, even the shape of both metallic lead surfaces may well be anything but regular and atomically flat. One therefore has to expect not only one specific but rather quite a variety of molecular alignments to be produced within one device. As one is interested in the conduction properties of the resulting device as a whole, it is important to understand the influence of each type of geometrical alignment to the transmission function.

To this end, we have investigated three such possible alignments, which will be discussed separately.

1. When metal atoms are added on top of the molecular monolayer in a random way, there might occur metallic clusters on top of the monolayer. These affect the electronic configuration of the molecules individually, and might therefore have an influence to the transmission function.
2. In a SAM experiment, there is not just one molecule, but rather a few hundred molecules involved. If the contribution to the transmission function was different for each molecule, then $T(E)$ would change qualitatively, with a change in size of the mono-layer. We therefore analyse how the transmission functions depends on the number of molecules involved.
3. The molecular monolayer may not be strictly periodic, but contain several defects. Within such a defect, the distance between two molecules can be reduced, such that inter-molecular interactions are enhanced. Each of these defects will have a specific electronic structure and will therefore influence the transmission function.

Influence of metallic clusters In the sandwich geometry, first the bottom metallic lead is created. Then the molecular mono-layer is adsorbed on top of it by self-assembly. Finally the top metallic lead is build upon the molecular mono-layer. The exact shape of neither metallic surface is known and may be anything but flat and regular.

It is likely that the surface atoms of the top metallic lead build up clusters on top of the molecular layer (as for example in Fig. 5.6 b). Which influence do they have on the electronic configuration of the molecule they are in contact with? And do the clusters act as small molecules with new electronic levels? In principle, there are three different influences which an Au cluster can have on the molecular-electronic structure: it introduces new electronic levels, the existing molecular-electronic levels can be shifted, and the coupling between molecule and lead is reduced due to a increase in spatial separation.

The effect of a reduced coupling to the lead can clearly be seen in Fig. 5.6 (c) where the amplitude of the transmission function is reduced with the Au cluster added. This result is in full agreement with DiVentra et al. (2000). However, the peak positions themselves are hardly affected. This was observed for several types of clusters similar to the one shown in Fig. 5.6 and indicates that the shift of the molecular levels only slightly depends

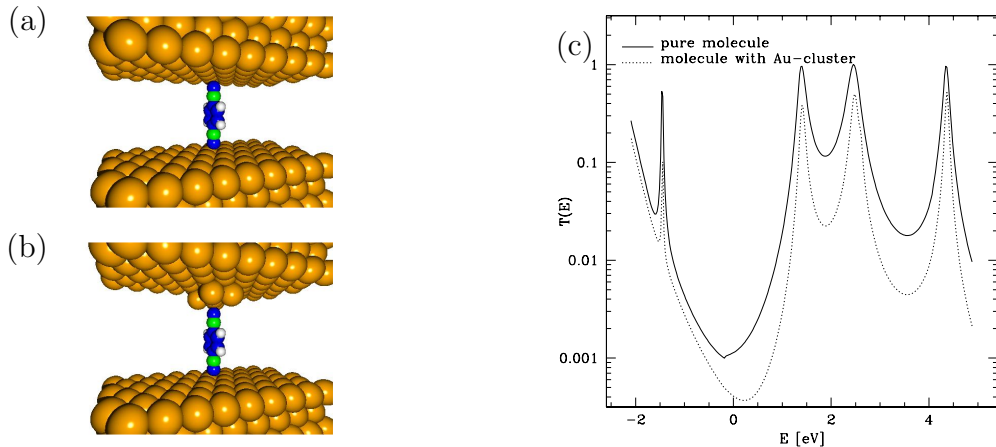


Figure 5.6: (a) Structure of a molecule without cluster. (b) Structure of a molecule with a gold cluster on top. (c) Transmission function $T(E)$ for both structures. The energy scale is relative to the HOMO-LUMO gap, such that $E = 0$ corresponds to the middle of the gap.

on the exact geometry of the neighbouring Au atoms. Finally, there are no additional peaks, which one might have expected because of the additional electronic levels of the cluster. The explanation of their absence is the following: an electronic level gives rise to a peak in the transmission function only if the corresponding orbital wave function overlaps with both the top and bottom electrode. The overlap with that electrode which the cluster is attached to (say top electrode) is of course large. The overlap with the bottom electrode consists of two parts. The direct overlap and the indirect overlap via the molecule. The direct overlap is negligible due to the large spatial separation. The indirect overlap is also negligible unless the energy of the cluster level coincides with a molecular energy level (otherwise there is no molecular level to overlap with). But in that case, there already exists a transmission peak due to the molecule itself.

In summary, if transmission is already suppressed by the molecule (at all off-resonant energies), it can either be further reduced by off-resonant tunnelling through the cluster, or it can (at best) be left unchanged by resonant tunnelling through the cluster. Under no circumstances can transmission, once suppressed by the molecule, be afterwards increased by the cluster. This in turn means that metallic clusters cannot give rise to additional peaks in the transmission spectrum.

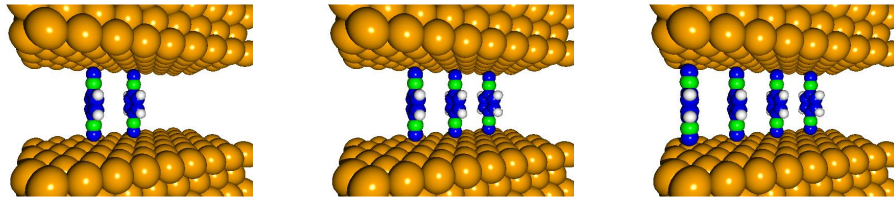


Figure 5.7: The structure of two, three, and four molecules adsorbed within an Au- 9×3 super cell. This setup was used to test the sum rule, Eq. (5.1). The results are shown in Fig. 5.8.

Mono-layer versus single molecule What do we expect the transmission function $T^i(E)$ for i periodically arranged molecules to look like? As long as the inter-molecular interactions are small (compared to the intra-molecular ones) the molecular levels of each molecule will not be significantly changed. Furthermore as the mono-layer consists of only one kind of molecule, all of them will have the same electronic structure. Therefore we expect each molecule to contribute roughly the same amount to the transmission function:

$$T^n(E) \approx \sum_i T^1(E) = nT^1(E), \quad (5.1)$$

where i runs over all n adsorbed molecules. We do not expect the equation to be fulfilled exactly, because the electronic structure of each molecule will always be slightly affected by the presence of neighbouring molecules.

We calculated the transmission function for $n=1$ to 4 molecules within an Au super cell of size 9×3 (the structures are shown in Fig. 5.7). The distance between the molecules is chosen to be a multiple of the closest Au-Au separation a_{Au} ($d = 5.76\text{\AA} = 2a_{\text{Au}}$, with $a_{\text{Au}} = 2.88\text{\AA}$). To our knowledge, the parameters of the PDI-SAM mono-layer have never been determined experimentally, which is why we have to assume the above values. However STM studies (Zeng et al., 2002) and also theoretical calculations (Yourdshahyan and Rappe, 2002) have been performed for alkanethiol mono-layers, and these parameters motivated our choice. According to structure optimisations the hollow-site adsorption is stronger than the top-site adsorption. The inter-molecular distance is taken from the observation of (Zeng et al., 2002).

As we have expected according to Eq. (5.1), the transmission functions have the same amount of peaks, independently from the number of molecules present and at identical energetic positions (see Fig. 5.8 a). This result is also

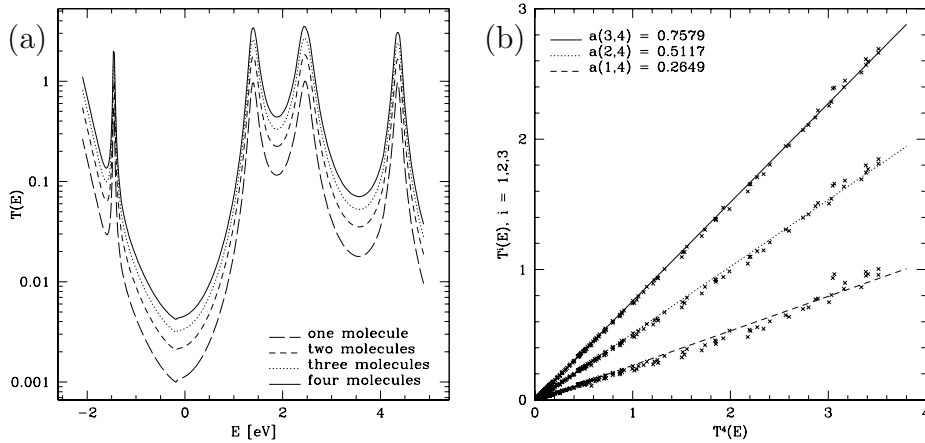


Figure 5.8: (a) Transmission function for one, two, three, and four PDI molecules (see Fig. 5.6 (a) and Fig. 5.8). (b) When plotted against each other, the transmission functions reveal a linear relationship: $T^i(E) = a(i, 4)T^4(E)$, where $a(i, 4) \approx \frac{i}{4}$.

obtained for all larger distances of the molecules, where the inter-molecular interaction is even smaller. Furthermore, the sum rule (Eq. 5.1) is indeed fulfilled, as shown in Fig. 5.8 (b), where each $T^i(E)$ is plotted against $T^4(E)$ for $i \in \{1, 2, 3\}$. The calculated transmission values (300 discrete values each) clearly show a linear correlation. The straight lines are linear fits to the data, and their slope does very well agree with the theoretically expected value of $a(n, m) = n/m$. The deviation is below 6%, as can be seen in table 5.1, where we summarise all the fitted values for $T^n(E) = a(n, m) \cdot T^m(E)$.

We conclude the following: a monolayer, in which the inter-molecular distance is large enough to not let inter-molecular interactions play a significant role, has the same number of distinct electronic levels as a single molecule. These levels are then highly degenerate. A *CV*-diagram will therefore have the same number of peaks. Only the net current will be increased by a factor $a(n, m)$ compared to the single molecule case. The mere fact that one deals with a mono-layer instead of a single molecule does not imply that the transmission function changes qualitatively.

Influence of molecular clusters We have seen that one does not observe additional peaks in the transmission function as long as the inter-molecular influence is small; this is the case for distances which occur in typical SAM structures (Zeng et al., 2002; Yourdshahyan and Rappe, 2002). We now investigate cases, in which the molecular interactions are not negligible. This

n	m	$a(n, m)$	$\frac{a}{n/m} - 1$	σ
1	2	0.5188	3.76%	0.014
1	3	0.3500	4.99%	0.018
1	4	0.2649	5.96%	0.021
2	3	0.6753	1.30%	0.008
2	4	0.5117	2.34%	0.015
3	4	0.7579	1.06%	0.011

Table 5.1: The fitted values for $a(n, m)$ together with their deviation from the theoretical value $a(n, m) := n/m$ and a measure for the quality of the fit σ , where $\sigma^2 := (N-1)^{-1} \sum (T^n(E_i) - a(n, m)T^m(E_i))^2$ for $N = 300$ discrete energy values $T(E_i)$.

occurs for example when the periodic structure of the mono-layer is perturbed by an additional molecule, such that a molecular cluster is formed. It is sufficient to study the transmission function of an isolated cluster only, because we have already seen that molecules in the periodic SAM arrangement do not influence each other. The sum of the transmission function for the periodic SAM and the transmission function for the molecular cluster is, due to the sum rule, the total transmission function for defect and SAM.

We study the influence of a shorter distance between two, three, and four molecules on the transmission spectrum and relate it to the discrete energies of the isolated molecules. The molecules are now separated by $d = 2.88\text{\AA}$ which corresponds to the Au-Au atom spacing a_{Au} . The atomic structure for this calculation is shown in Fig. 5.9 (a), the resulting transmission functions in Fig. 5.9 (b) and (c).

Upon reducing the molecular separation from $d_1 = 2a_{\text{Au}}$ to $d_2 = a_{\text{Au}}$, the transmission function qualitatively changes: the number of peaks roughly doubles, and the new peak positions are different from the ones we have obtained in the previous calculations and do depend on the number of molecules involved. This is an important point, because if there are several molecular clusters with different molecular distances, then they all give rise to peaks at different energy values. The resulting transmission function is the sum of the individual functions and will thus contain far more peaks than the transmission function for the non perturbed periodic layer.

We now show that the new peaks are a result of the increase in molecular interaction due to the decrease in spatial separation. For non-interacting molecules, the molecular energies are identical and therefore degenerate. An interaction between molecules breaks this degeneracy, and therefore new en-

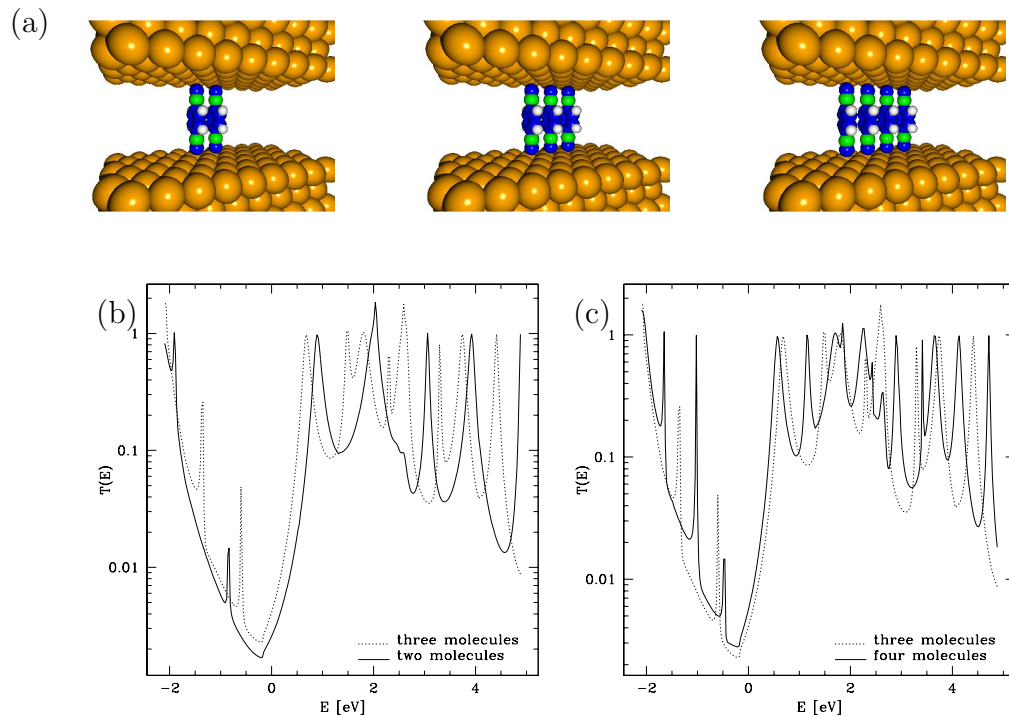


Figure 5.9: (a) Two, three, and four molecules with a short inter-molecular distance of $d = a_{\text{Au}} = 2.88\text{\AA}$. (b) The transmission functions for two and three molecules. (c) The transmission functions for three and four molecules. In contrast to all previous cases, the peaks are shifted with respect to each other and there are also additional peaks. These changes are due to the increase in inter-molecular interaction, which alters the electronic levels.

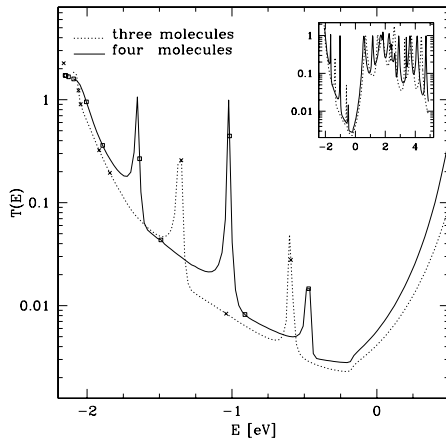


Figure 5.10: Magnification of the transmission functions for three and four closely spaced molecules from Fig. 5.9 (c). Additionally the discrete energy levels of the molecular region are plotted as points along the transmission function. There corresponds at least one discrete energy level to each peak. A detailed discussion is given in the main text. Inset: Transmission function (original scale) for three and four closely spaced molecules (identical to Fig. 5.9 c).

ergy levels occur. By performing a diagonalisation of the molecular Hamiltonian (without leads), one can determine the levels of the molecular cluster.

In Fig. 5.10 we have again plotted the transmission function for three and four molecules, this time together with the discrete energy levels of the corresponding molecular cluster. The inset is identical to Fig. 5.9 (c), while the plot itself is a magnification, to better resolve the discrete energy levels (which are shown as points along the transmission function). Each of the transmission peaks is related to at least one discrete energy value. But the reverse statement is not true: not each energy value can be related to a peak in the transmission function. Why is that? The discrete energies can only give rise to new peaks in the transmission function if they are not suppressed by a weak coupling to one of the leads. All levels which are not related to any peak belong to this category. If the position of the peak is shifted away from a corresponding energy level, then this is due to the coupling between molecules and leads. This coupling is absent in the diagonalisation of the molecular Hamiltonian, but is automatically included in the calculation of the transmission function.

Finally we show that the additional peak structure in the transmission

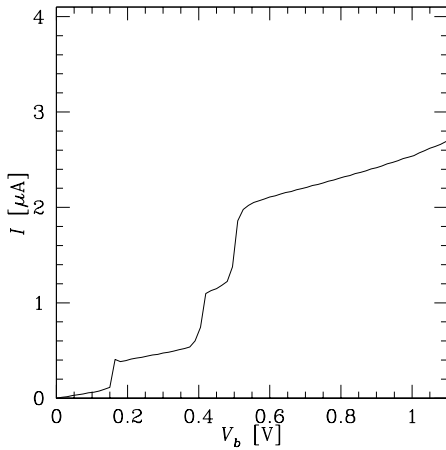


Figure 5.11: IV -calculation for a molecular region containing all three molecular clusters shown in Fig. 5.9 (a). There are three distinct steps within the voltage range of 1V.

function for a scenario with an increased inter-molecular interaction gives rise to a number of steps in the IV -curve. Figure 5.11 contains an IV calculation for a molecular structure containing all three molecular clusters shown in Fig. 5.9 (a). In this calculation, the bias voltage V enters as a shift of the Fermi levels for source and drain lead: $\mu_1 = \mu_2 + eV$. The molecular energy has been set to $E_m = \mu_1 - \delta E_m - \eta eV$, where δE_m is the zero bias displacement of the molecular levels and $\eta = 0.5$, because of the symmetric coupling to the leads.

Compared to the experiments by Lee et al. (2003) and Dupraz et al. (2003) the number of steps in the IV -curve is well reproduced by our calculation. The obtained current is at least one order of magnitude larger than the experimental values. This is a phenomenon common to all theoretical methods based on the Landauer formula (Emberly and Kirczenow, 2001; Bauschlicher et al., 2003). A satisfactory explanation for this discrepancy as well as for the broad range of experimentally observed current values has not yet been found.

5.4.3 Discussion

We have shown that the peak structure of the transmission function is robust against changes in the number of adsorbed molecules, as long as the distance between molecules is considerably large ($d \gtrsim 6\text{\AA}$). And also does

the exact shape of the top metallic lead not influence the qualitative structure of the transmission function. Only if the distance between molecules becomes comparable to atomic length scales, inter-molecular interactions are no longer negligible and the transmission function undergoes a qualitative change. Namely an additional peak structure occurs.

How does this finding compare to the experimental data? As we have pointed out in section 5.3, a more or less random peak structure was observed in the *CV* characteristic only in devices using molecules with two isocyanide groups (Lee et al., 2003; Dupraz et al., 2003). In other devices molecules with at least one thiol group are typically used. These show significantly less peak structure.

We therefore give the following interpretation: The thiol group is known to bind strongly to Au atoms. It is therefore likely, that thiol-based monolayers stably adsorb to gold leads. Resulting periodic structures are then robust against distortions. The conductance of such structures is proportional to the corresponding single molecule conductance, i.e. the number of molecules involved changes the absolute value of the current only, not the peak structure.

The random like peak structure in devices made up of isocyanide based molecules suggests that there are molecular clusters present in the monolayer. These clusters might occur because the binding of an isocyanide group to Au is considerably weaker compared to that of a thiol group, and weaker binding results in a less robust periodic structure.

Chapter 6

Understanding STM images

In this chapter we present another application of the numerical method which we have implemented, namely the calculation of scanning tunnelling microscope (STM) images. Starting with an historical overview and a short introduction into the working principle of an STM, we consider experiments which can only be understood in accordance with theoretical calculations beyond the Tersoff-Hamann approximation. We also present our own calculations from a cooperation with Constable et al. (2004) to support the interpretation of recent STM images. As the system under investigation is considerably large, we were able to produce the numerical images only by introducing a special treatment for a large eigenvalue problem, which cannot be solved sufficiently accurately by conventional methods. This is the first time that a method has been implemented that can perform image calculations for a system of that size.

6.1 Introduction

This section provides an introduction to the STM with respect to its history, its working principle, and some of its applications. We focus on experimental aspects here, as the approaches in use to numerically calculate transport through molecular systems have already been discussed (see Chap. 2 and 4). Detailed reviews about theories specific to the STM can also be found in the literature (Briggs and Fisher, 1999; Hofer and Foster, 2003).

6.1.1 Historical overview

The optical microscope can be used to obtain real-space images of structures which are too small to be visible to the unaided eye. However, its resolution

is restricted to objects larger than half the width of the wavelength of visible light (i.e. larger than roughly 250nm). Even smaller objects can be viewed using electron microscopy. The transmission electron microscope (invented by Knoll and Ruska, 1932a,b) detects electrons from a beam that was transmitted through the sample while the scanning electron microscope detects secondary electrons which are emitted from the surface due to excitation by a primary electron beam. Both methods are capable of resolving objects down to the scale of several nanometers by using electron beams with a wavelength considerably smaller than that of visible light. They are invasive methods, because the highly energetic electron beam has to be directed onto and interact with the sample. Furthermore, the samples have to be viewed in vacuum to prevent the electrons from being scattered by air.

In 1981 the scanning tunnelling microscope was invented by Binnig et al. (1981, 1982). It was the first tool that allowed real-space images of surfaces to be obtained with atomic resolution and its inventors Gerd Binnig and Heinrich Rohrer were jointly awarded half of the 1986 Nobel Prize in Physics¹. The STM is widely used in both industrial and fundamental research where it serves as an instrument for analysing bare surfaces, adsorbates on top of surfaces and also for manipulating these adsorbates on the nanometer scale (Bartels et al., 1997). It can be operated at room temperature and atmospheric pressure although higher resolution is obtained under ultra-high vacuum conditions.

6.1.2 Working principle

Figure 6.1 shows a typical STM setup. An atomically sharp metallic tip is approached to the surface under investigation. When the distance z between surface and tip is small enough ($z < 10\text{\AA}$) there is a measurable probability for electrons to tunnel between tip and surface and vice versa. With an applied voltage U the chemical potential of (say) the tip μ_2 is lowered relative to the chemical potential of the substrate μ_1 , and therefore each electron that has tunnelled into the tip will equilibrate within the tip-bulk, thereby contributing to a tunnelling current. This current depends

- on the exact position of the tip,
- on the applied voltage,
- on the type of tip, surface, and (if present) adsorbate material,

¹The other half was awarded to Ernst Ruska for his invention of the electron microscope.

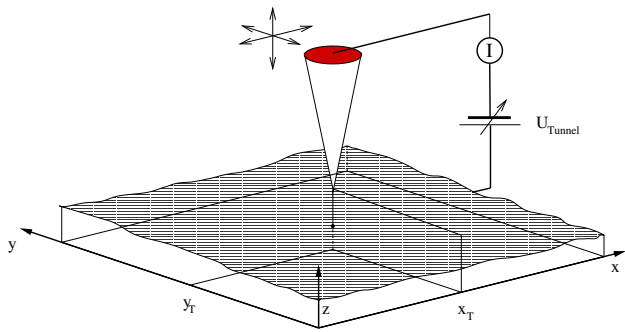


Figure 6.1: The working principle of an STM device (taken from Aschauer, 1999). Tip and surface are biased via an applied voltage in order to record a small tunnelling current which depends on the tip position.

- as well as on several laboratory conditions such as temperature, pressure etc.

Because of the extreme sensitivity of the tunnelling current to the tip position one can generate topographic surface images by scanning in lateral direction over the sample. Thereby two different modes are possible. Surfaces which are known to be atomically flat can be scanned in the constant-height mode, where the tunnelling current is measured as a function of lateral position and fixed tip-surface distance z : $I = I(x, y, z = \text{const})$. The second mode is the so-called constant-current mode, where during the scan across the surface the tip-height is adjusted by a feedback loop, to fix the tunnelling current at a chosen value. The different values for the tip height are recorded and make up the STM image: $z = z(x, y, I = \text{const})$. This latter mode is typically used when the surface structure is either not known or known to not be entirely flat.

There is a third mode for STM operation which differs from the above mentioned ones in that it is not only used to image the surface but also to manipulate the position of adsorbed molecules. This can be achieved by decreasing the tip-surface distance in the vicinity of the molecule below a certain critical value at which the tip influence becomes irreversible. When one deals with adsorbates building molecular monolayers, this can result in the removal of a single molecule, i.e. it constitutes a controlled write operation. With the above mentioned reversible constant-current mode a read-only operation can also be performed.

These capabilities of the STM motivated intensive research within the last decade aiming to build memory storage devices on the molecular or even atomic level (Miller et al., 1997; Bennewitz et al., 2002). Nevertheless we

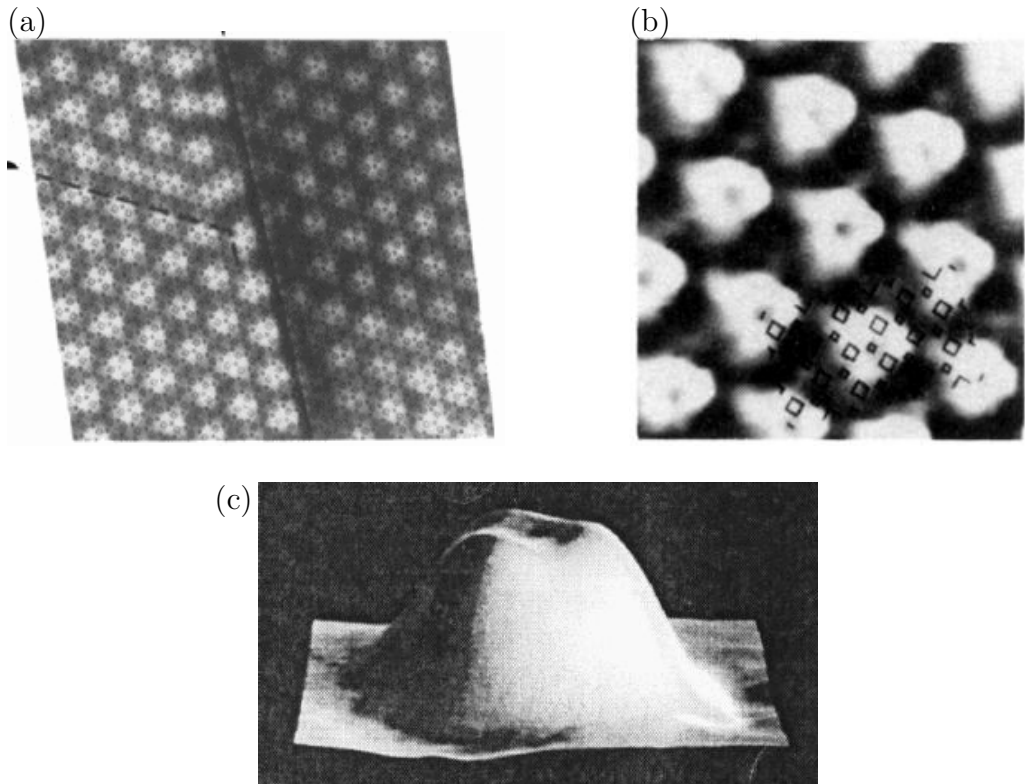


Figure 6.2: A collection of images taken with an STM: (a) image of Rhodium surface $^{103}\text{Rh}(111)$ (taken from Ohtani et al., 1988) (b) same surface with benzene molecules (C_6H_6) adsorbed (taken from Ohtani et al., 1988) (c) benzene adsorbed on Platinum $^{195}\text{Pt}(111)$ (taken from Weiss and Eigler, 1993).

restrict ourselves to reversible STM applications from now on.

6.1.3 Examples of STM images

A few representative images taken with an STM are shown in Fig. 6.2. By scanning over clean surfaces, the orientation of the top layer can be determined. In Fig. 6.2 (a) a step in the surface layer of Rh(111) can be identified. The image changes drastically when an adsorbate is present. In Fig. 6.2 (b) the same surface is shown, this time with benzene molecules adsorbed on top. They appear as hills with a dip in the middle. Another image of benzene, but adsorbed on Pt(111) and with a much higher resolution, is shown in Fig. 6.2 (c).

6.2 Numerical STM image calculations

As the STM technique was more and more established, it became obvious that there are reproducible experimental effects which can not be explained by the Tersoff-Hamann formula (see Sec. 2.1.3 and 2.1.4). In these cases, the underlying assumption that any influence of the tip can be ignored is no longer justified. This section is devoted to cases in which it was necessary to perform numerical calculations beyond the Tersoff-Hamann approximation in order to explain experimental observations.

6.2.1 Image contrast inversion

Doyen et al. (1993) were able to show that the experimentally observed effect of image contrast inversion (Kopatzki and Behm, 1991; Schuster et al., 1991) can be explained by the influence of the tip potential at short tip-surface distances. They considered a bare metallic Palladium (Pd) surface.

First they calculated the local electronic density of states for the bare surface using DFT. Thereby they confirmed that it takes a maximum value on top of a Pd surface atom, independently of the distance z from the surface. Above the hollow site the electronic density takes a minimum value.

In a second step, the STM tunnelling current was calculated. This was done using scattering theory for a periodically repeated Pd slab. The tip was modelled via a localised attractive potential. They found that the local extrema of the tunnelling current coincide with the extrema of the density of states only for tip-surface distances larger than 3 Å. For closer distances the image contrast undergoes an inversion, and maxima of the tunnelling current correspond to minima of the density of states. This image contrast inversion is shown in Fig. 6.3.

This effect can be explained as follows. With decreasing tip-surface distance, the increasing interaction between the resonance state of the localised tip potential and the delocalised surface states yields a splitting into bonding and anti-bonding states. Because of the d -type orbital structure of Pd this interaction is stronger for the hollow site than for the top site and so is the splitting. The stronger bonding then results in a larger current for the hollow site compared to the top site.

6.2.2 Negative differential resistance

Another example for the important influence of the tip electronic structure is the occurrence of negative differential resistance (NDR) in scanning tunnelling spectroscopy experiments. In those experiments the bias voltage is

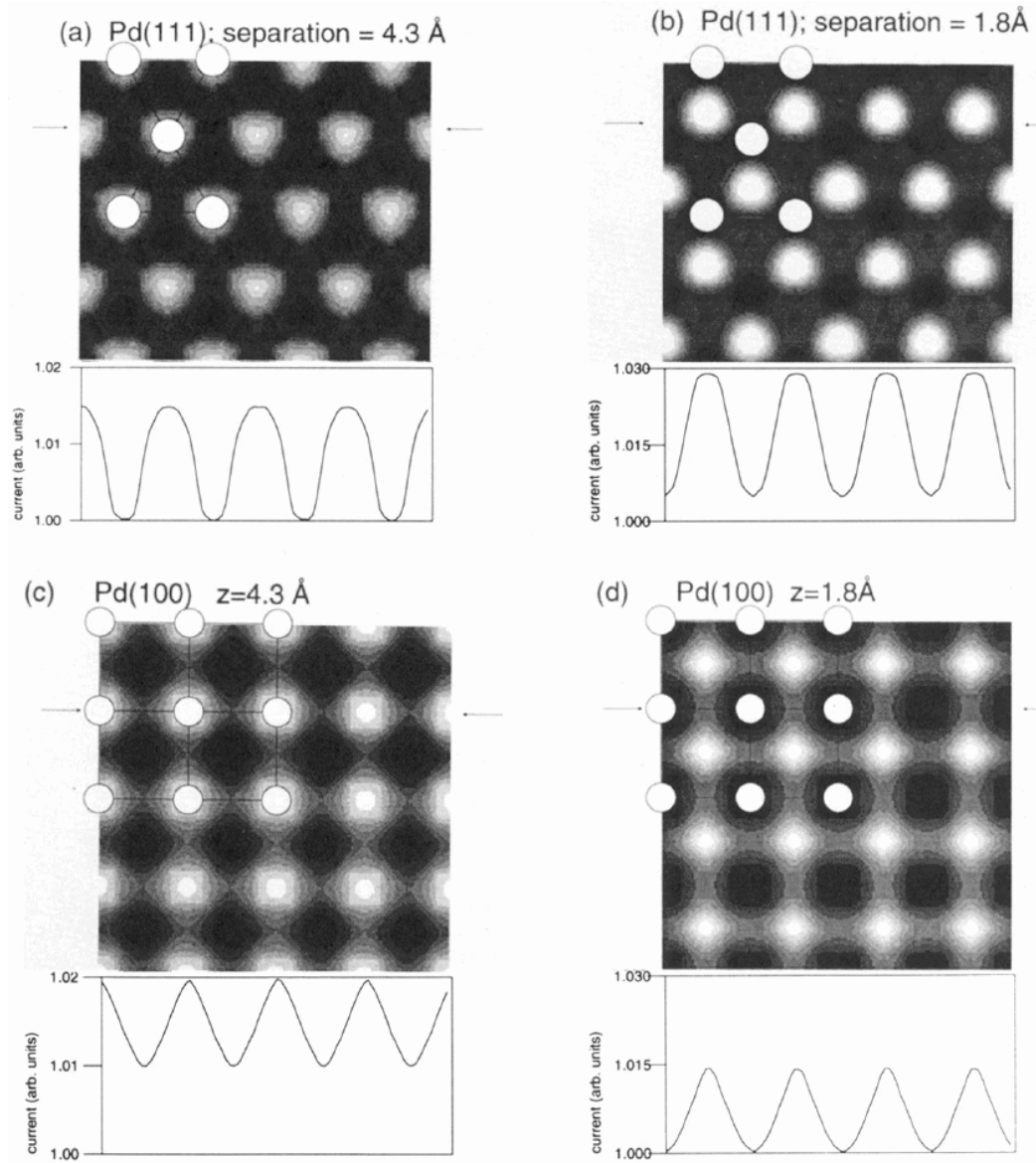


Figure 6.3: Calculation of the tunnelling current for two different distances of the STM tip. The image contrast undergoes an inversion (i.e. current maxima become minima and vice versa) when the tip-surface distance is decreased (taken from Doyen et al., 1993).

tuned while the STM tip position is not changed. In this way the conductance properties $G(V) = dI/dV$ of specific points above the surface can be measured.

Negative differential resistance cannot be explained within the Tersoff-Hamann approximation because the tunnelling current is taken to be directly proportional to the applied voltage, such that the conductance is always positive and constant.

Tsukada et al. (1991) addressed the phenomenon of NDR by using the Bardeen formula together with first-principles electronic structure calculations, which they performed for substrate and tip. Within their calculations NDR occurred only when the STM current was dominantly produced by the tunnelling between a single tip state and a single substrate state both close to the Fermi energy.

The mechanism of NDR is the following: for increasing but still small applied bias voltages, the broadening of the energy window which is being integrated over in the Bardeen formula, results in an increase of the tunnelling current. Thus the conductance must be positive. By further increasing the bias voltage, the Fermi level offset between substrate and tip drives the two states dominating the current off resonance. This leads to a decrease in the tunnelling matrix element M_{ij} , because it involves the product of the LDOS of each of the two states, which is much reduced if the peak positions of the two LDOSs are shifted apart. A decrease of the total current and therefore a negative differential resistance is then obtained.

6.2.3 Electric field effects

The tip-induced electric field at the surface is, assuming a tip-sample separation of $5 - 10\text{\AA}$ and an applied voltage of $1V$, of the order of 10^9Vm^{-1} . Such an electric field can be expected to have a considerable effect onto the electronic structure of the surface when its polarisability changes with spatial position. This is for example the case when hydrocarbons, which are only slightly polarisable ($\epsilon_r \approx 2$), are adsorbed on silicon ($\epsilon_r \approx 14$) (Briggs and Fisher, 1999).

When STM data from the bare silicon surface (Tromp et al., 1985) and from hydrocarbons adsorbed on silicon (Mayne et al., 1993) were compared, it was found that, although the molecules are adsorbed on top of the silicon surface, they appear lower than the bare silicon surface dimers in the constant current mode image. This can be explained by the influence of the tip induced electric field, which effectively pulls the electrons out of the regions with a higher polarisability.

Numerical simulations neglecting the tip-induced electric field result in

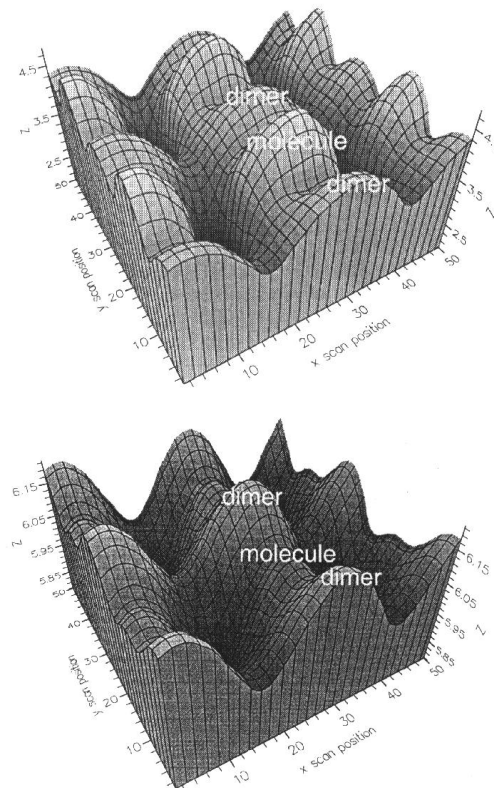


Figure 6.4: Influence of the tip-induced electric field. The apparent height of an adsorbed molecule can be changed. Hydrocarbons adsorbed on silicon appear as bumps (top figure) in calculations neglecting the electric field. In contrast, when accounting for the field the adsorbed molecules correspond to lower regions of the STM image (bottom figure), in accordance with experiment (Ness and Fisher, 1997).

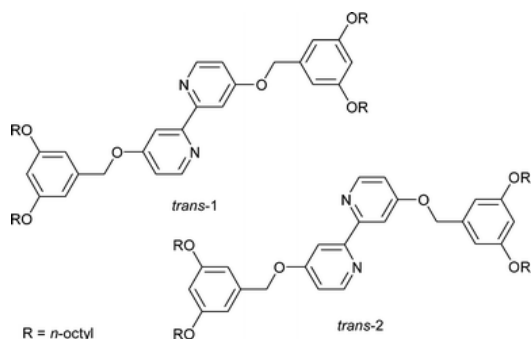


Figure 6.5: The two conformations of the molecule investigated by Constable et al. (2004).

images where the adsorbed molecules appear to be higher than the bare silicon dimers. Only when the electric field is taken into account do the calculations agree with experiment (Ness and Fisher, 1997).

6.2.4 Conformational analysis of self-organised monolayers

The search for molecular structures which self-organise on substrate surfaces in a controllable way is currently a hot topic in material science. It is research which combines the work of both chemists and physicists. Chemists are concerned with synthesising molecules with self-organising capabilities along with special properties like the stable adsorption on surfaces. Physicists then perform STM studies of the resulting structures, thereby confirming or invalidating the properties of interest.

Experimental observations

Constable et al. (2004) are studying molecular systems that exhibit multiple conformations on a graphite surface (see Fig. 6.5). This knowledge is taken from STM studies which show multiple domains. There are two sets of these domains with an angular relation of 6.5° (see Fig. 6.6). As there was used only a single molecular type, the domains have to correspond to different conformations of this molecule. Now the question arises how the domains can be mapped to different conformations.

Because the STM images are obtained with sub-molecular resolution, different conformations can be tested with respect to a possible packing arrangement matching the periodic structure present in the STM image. Thereby

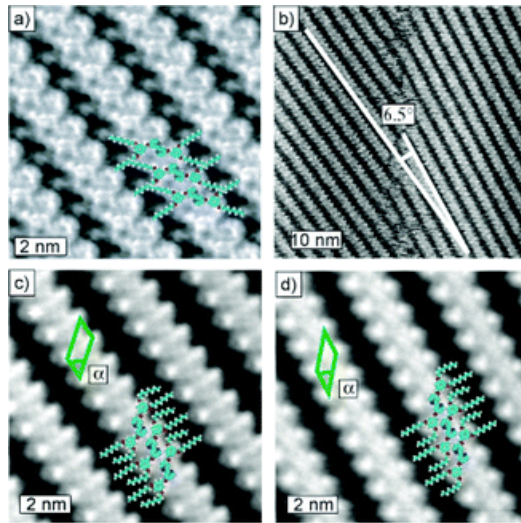


Figure 6.6: (a) Packing arrangement for *trans*-2 conformation. (b) STM image of two domains differing in orientation by an angle of 6.5° . (c) Expanded image of the domain corresponding to the *trans*-2 configuration. (d) Expanded image corresponding to the *trans*-1 configuration (images taken from Constable et al., 2004).

Constable et al. (2004) were able to uniquely relate each domain to a single conformation (see Fig. 6.6).

However, details of the conformation concerning the angular direction of the bond between oxygen atom and the attached hydrocarbon chains (named R in Fig. 6.5) remain unknown. Two different conformations are shown in Fig. 6.7. Because the hydrocarbon chains do not show up in the STM images explicitly, both conformations can be matched with the experiment. But it is believed that they give rise to different sub-molecular structures in the images. Calculations can be used to predict the sub-molecular structure and by comparing the theoretical images with the ones obtained experimentally, it may be possible to pin down the conformational structure more strictly.

However, the algorithms for calculating STM images are limited to small systems, at least systems too small to contain the molecule of interest (Fig. 6.7) and to our knowledge, no calculations have ever been published for a molecule of comparable size. This was also true for the ESQC method. Yet we figured out the bottle neck of the calculation and by reformulating the corresponding mathematical problem we succeeded in extending the method to systems large enough for the molecule to fit into.

Theoretical calculations

Because the molecule is wide spread on top of the graphite surface, a very large super cell has to be used. The size of this super cell in turn determines the dimension of the propagator matrix which enters the ESQC algorithm. This non-symmetric matrix has to be diagonalised, in order to obtain the propagating channels (see Chap. 4). A straight forward diagonalisation using standard linear-algebra packages (LAPACK) proved to result in inaccurate eigenvalues. This affects the algorithm in a dramatic way: a significant loss in accuracy of the eigenvalues renders the entire method useless. This is because each eigenvalue, depending on its modulus, corresponds to a propagating or an evanescent incoming or outgoing solution. The method relies on an identical amount of incoming and outgoing solutions. Below a certain numerical accuracy such an equal partitioning is no longer possible, resulting in the breakdown of the method.

By using the periodic nature in lateral direction of each lead explicitly, we were able to transform the diagonalisation procedure from a single step diagonalisation of a large quadratic $2NM$ matrix into N individual diagonalisation steps each involving a $2M$ dimensional quadratic matrix only. Here N corresponds to the size of the super cell in units of the unit cell and M is the number of (valence) electrons contained in the latter. As M is independent of the system size (super cell size), so is the accuracy of the diagonalisation step.

Only after the implementation of this exceedingly more accurate diagonalisation procedure was it possible to consider a super cell large enough for the molecule to fit in. The remaining restriction is now imposed by the available computer memory (RAM). This allows, for the first time, theoretical studies of such large molecules adsorbed on surfaces while still using an atomic description of the entire system.

Currently we are considering several conformations (two of which are shown in Fig. 6.7) of the molecules possibly involved in the above mentioned experiments. Preliminary results are presented in Fig. 6.8. Each image is obtained by scanning a region of size $30 \times 50 \text{ \AA}^2$ with a resolution of 60×100 points. As the calculation for a single point takes roughly 4 minutes on a present-date PC, the total computer time for an entire image amounts to almost two and a half weeks.

These calculations have to be considered as work in progress. So far we have merely proven that calculations of this type are possible from a technical point of view. Whether at all and for which parameter range the calculations are in accordance with experiments remains to be seen. Further studies concerning the influence of parameters like molecule-substrate distance, tip-

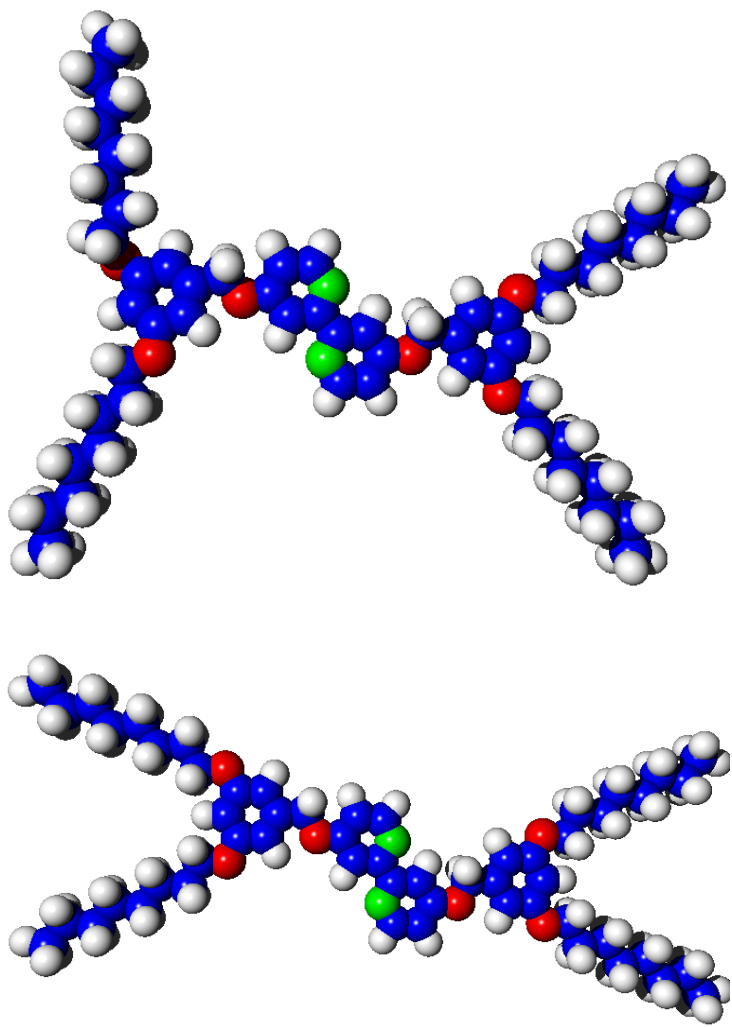


Figure 6.7: Two different conformations of the molecule investigated by Constable et al. (2004). They enter as input to STM image calculations (see Fig. 6.8).

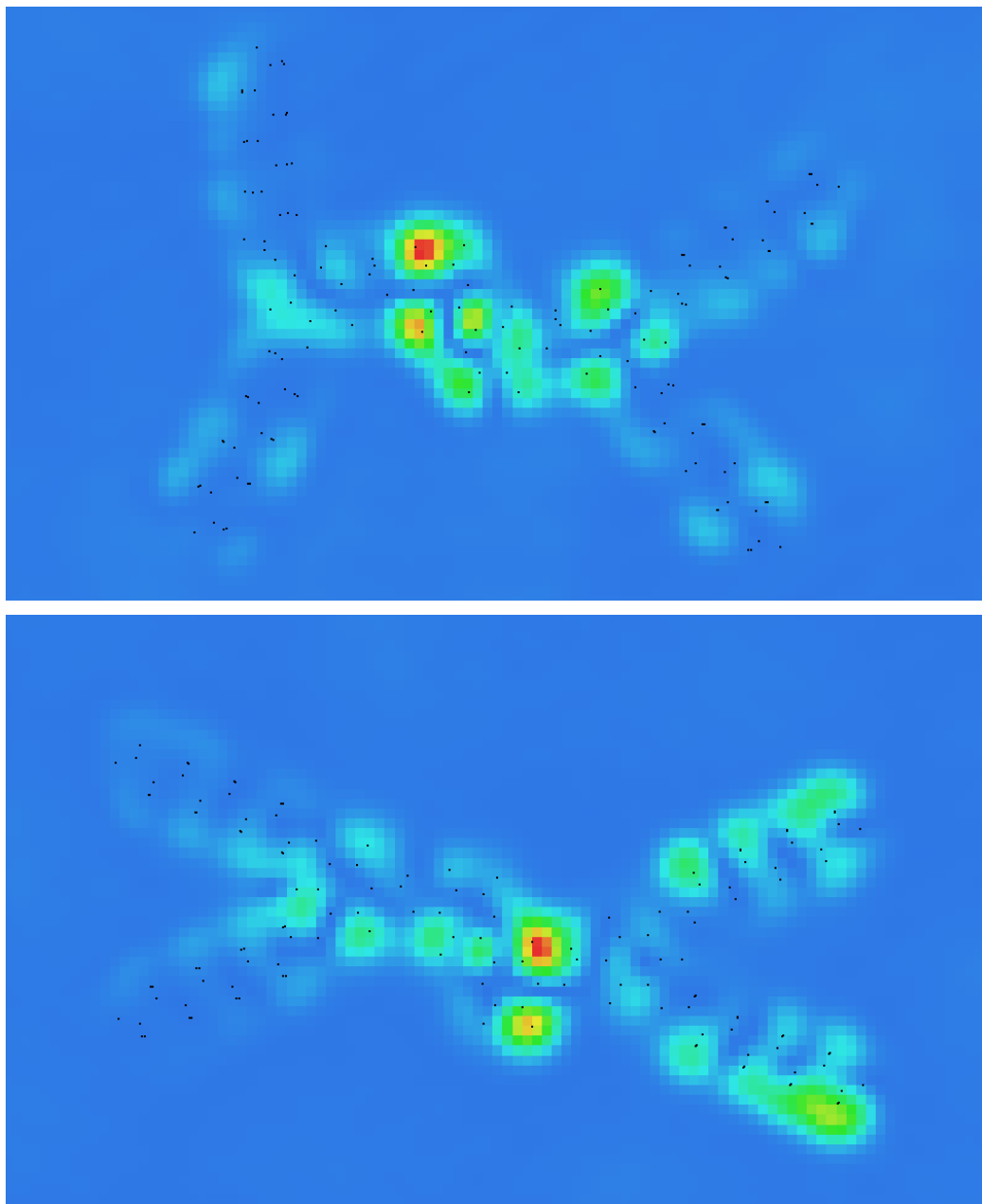


Figure 6.8: Sample STM image calculations for two different conformations of the same molecule (which are shown in Fig. 6.7). The projected atomic positions are plotted as black pixels, irrespective of their chemical type. Further studies are in order to finally perform calculations which can be related directly to the experiments.

surface separation and molecule-surface orientation are in order to finally perform calculations which can be related directly to the experiments. This is part of the future work which arises from the present thesis.

Bibliography

- Aschauer, H. (1999). Scanrichtungsabhängigkeit bei STM-Aufnahmen von Adsorbaten. Master's thesis, LMU-München. In German.
- Aviram, A. and Ratner, M. A. (1974). Molecular rectifiers. *Chemical Physics Letters*, 29(2):277–283.
- Bardeen, J. (1961). Tunneling from a Many-Particle Point of View. *Physical Review Letters*, 6(2):57–59.
- Bartels, L., Meyer, G., and Rieder, K.-H. (1997). Basic Steps of Lateral Manipulation of Single Atoms and Diatomic Clusters with a Scanning Tunneling Microscope Tip. *Physical Review Letters*, 79(4):697–700.
- Bauschlicher, C. W., Ricca, A., Mingo, N., and Lawson, J. (2003). On the current flow for benzene-1,4-dithiol between two Au contacts. *Chemical Physics Letters*, 372(5-6):723–727.
- Bennewitz, R., Crain, J. N., Kirakosian, A., Lin, J.-L., McChesney, J. L., Petrovykh, D. Y., and Himpel, F. J. (2002). Atomic scale memory at a silicon surface. *Nanotechnology*, 13:499–502.
- Bingham, R. C., Dewar, M. J. S., and Lo, D. H. (1975a). Ground states of molecules. XXV. MINDO/3. Improved version of the MINDO semiempirical SCF-MO method. *Journal of the American Chemical Society*, 97(6):1285–129.
- Bingham, R. C., Dewar, M. J. S., and Lo, D. H. (1975b). Ground states of molecules. XXVI. MINDO/3 calculations for hydrocarbons. *Journal of the American Chemical Society*, 97(6):1294–1301.
- Bingham, R. C., Dewar, M. J. S., and Lo, D. H. (1975c). Ground states of molecules. XXVII. MINDO/3 calculations for carbon, hydrogen, oxygen, and nitrogen species. *Journal of the American Chemical Society*, 97(6):1302–1306.

- Bingham, R. C., Dewar, M. J. S., and Lo, D. H. (1975d). Ground states of molecules. XXVIII. MINDO/3 calculations for compounds containing carbon, hydrogen, fluorine, and chlorine. *Journal of the American Chemical Society*, 97(6):1307–1311.
- Binnig, G., Rohrer, H., Gerber, C., and Weibel, E. (1981). Tunneling through a controllable vacuum gap. *Applied Physics Letters*, 40(2):178–180.
- Binnig, G., Rohrer, H., Gerber, C., and Weibel, E. (1982). Surface Studies by Scanning Tunneling Microscopy. *Physical Review Letters*, 49(1):57–61.
- Born, M. and Oppenheimer, J. R. (1927). Zur Quantentheorie der Moleküle. *Annalen der Physik*, 84(20):457–484.
- Brandbyge, M., Mozos, J.-L., Ordejon, P., Taylor, J., and Stokbro, K. (2002). Density functional method for nonequilibrium electron transport. *Physical Review B*, 65:165401.
- Briggs, G. and Fisher, A. (1999). STM experiment and atomistic modelling hand in hand: individual molecules on semiconductor surfaces. *Surface Science Reports*, 33(1-2):3–81.
- Büttiker, M., Imry, Y., Landauer, R., and Pinhas, S. (1985). Generalized many-channel conductance formula with application to small rings. *Physical Review B*, 31(10):6207–6215.
- Chen, C. J. (1990a). Origin of atomic resolution on metal surfaces in scanning tunneling microscopy. *Physical Review Letters*, 65(4):448–451.
- Chen, C. J. (1990b). Tunneling matrix elements in three-dimensional space: The derivative rule and the sum rule. *Physical Review B*, 42(14):8841–8857.
- Chen, J., Reed, M. A., Rawlett, A. M., and Tour, J. M. (1999). Large On-Off Ratios and Negative Differential Resistance in a Molecular Electronic Device. *Science*, 286(5444):1550–1552.
- Constable, E. C., Hermann, B. A., Housecroft, C. E., Merz, L., and Scherer, L. J. (2004). Monitoring conformational diversity in self-organised monolayers with scanning tunnelling microscopy at near atomic resolution. *Chemical Communications*, (8):928–929.
- Dahlke, R. and Schollwöck, U. (2004). Electronic transport calculations for self-assembled monolayers of 1,4-phenylene diisocyanide on Au(111) contacts. *Physical Review B*, 69(8):085324.

- Darosa, P. A. and Seminario, J. M. (2001). Electron Transport through Single Molecules: Scattering Treatment Using Density Functional and Green Functions Theories. *Journal of Physics C*, 105:471–481.
- Datta, S. (1995). *Electronic Transport in Mesoscopic Systems*. Cambridge University Press, Cambridge, U. K.
- Dewar, M. J. S. and Thiel, W. (1977). Ground states of molecules. 38. The MNDO method. Approximations and parameters. *Journal of the American Chemical Society*, 99(15):4899–4907.
- Dewar, M. J. S., Zoebisch, E. G., Healy, E. F., and Stewart, J. J. P. (1985). Development and use of quantum mechanical molecular models. 76. AM1: a new general purpose quantum mechanical molecular model. *Journal of the American Chemical Society*, 107(13):3902–3909.
- DiVentra, M., Pantelides, S. T., and Lang, N. D. (2000). First-Principles Calculation of Transport Properties of a Molecular Device. *Physical Review Letters*, 84(5):979–982.
- Doyen, G., Drakova, D., and Scheffler, M. (1993). Green-function theory of scanning tunneling microscopy: Tunneling current and current density for clean metal surfaces. *Physical Review B*, 47(15):9778–9790.
- Drude, P. K. L. (1900a). Zur Elektronentheorie der Metalle. *Annalen der Physik*, 1(3):566–614.
- Drude, P. K. L. (1900b). Zur Elektronentheorie der Metalle. II. Teil. *Annalen der Physik*, 3(11):369–403.
- Dupraz, C. J. F., Beierlein, U., and Kotthaus, J. P. (2003). Low Temperature Conductance Measurements of Self-Assembled Monolayers of 1,4-Phenylene Diisocyanide. *ChemPhysChem*, 4(11):1247–1252.
- Emberly, E. G. and Kirczenow, G. (2001). Models of electron transport through organic molecular monolayers self-assembled on nanoscale metallic contacts. *Physical Review B*, 64(23):235412–235419.
- Fisher, D. S. and Lee, P. A. (1981). Relation between conductivity and transmission matrix. *Physical Review B*, 23(12):6851–6854.
- Foresman, J. B. and Frisch, ÅE. (1996). *Exploring Chemistry with Electronic Structure Methods*. Gaussian, Inc. Pittsburgh, USA, second edition.

- Geddes, N. J., Sambles, J. R., Jarvis, D. J., Parker, W. G., and Sandman, D. J. (1990). Fabrication and investigation of asymmetric current-voltage characteristics of a metal/langmuir–blodgett monolayer/metal structure. *Applied Physics Letters*, 56(19):1916–1918.
- Hückel, E. (1931a). Quantentheoretische Beiträge zum Benzolproblem. I. Die Elektronenkonfiguration des Benzols und verwandter Verbindungen. *Zeitschrift für Physik*, 70:204–286.
- Hückel, E. (1931b). Quantentheoretische Beiträge zum Benzolproblem. II. Quantentheorie der induzierten Polaritäten. *Zeitschrift für Physik*, 72:310–337.
- Hückel, E. (1932). Quantentheoretische Beiträge zum Problem der aromatischen und ungesättigten Verbindungen. III. *Zeitschrift für Physik*, 76:628–648.
- Hückel, E. (1933). Die freien Radikale der organischen Chemie. Quantentheoretische Beiträge zum Problem der aromatischen und ungesättigten Verbindungen. IV. *Zeitschrift für Physik*, 83:632–668.
- Hückel, E. (1937a). Grundzüge der Theorie ungesättigter und aromatischer Verbindungen. *Zeitschrift für Elektrochemie*, 43:752–788.
- Hückel, E. (1937b). Grundzüge der Theorie ungesättigter und aromatischer Verbindungen. *Zeitschrift für Elektrochemie*, 43:827–849.
- Hettler, M., Schoeller, H., and Wenzel, W. (2002). Non-linear transport through a molecular nanojunction. *Europhysics Letters*, 57(4):571–577.
- Hettler, M. H., Wenzel, W., Wegewijs, M. R., and Schoeller, H. (2003). Current Collapse in Tunneling Transport through Benzene. *Physical Review Letters*, 90(7):076805.
- Hofer, W. A. and Foster, A. S. (2003). Theories of scanning probe microscopes at the atomic scale. *Reviews of Modern Physics*, 75(4):1287–1331.
- Hoffmann, R. (1962). Theory of Polyhedral Molecules. I. Physical Factorizations of the Secular Equation. *The Journal of Chemical Physics*, 36(2):2179–2189.
- Hoffmann, R. (1963). An Extended Hückel Theory. I. Hydrocarbons. *The Journal of Chemical Physics*, 39(1):1397–1412.

- Hohenberg, P. and Kohn, W. (1964). Inhomogeneous Electron Gas. *Physical Review B*, 136(3):B864–B871.
- Knoll, M. and Ruska, E. (1932a). Beitrag zur geometrischen Elektronenoptik I. *Annalen der Physik*, 12:607–640.
- Knoll, M. and Ruska, E. (1932b). Beitrag zur geometrischen Elektronenoptik II. *Annalen der Physik*, 12:641–661.
- Kohn, W. (1999). Nobel Lecture: Electronic structure of matter – wave functions and density functionals. *Reviews of Modern Physics*, 71(5):1253–1266.
- Kohn, W. and Sham, L. J. (1965). Self-Consistent Equations Including Exchange and Correlation Effects. *Physical Review*, 140(4A):A1133–A1138.
- Komiya, S., Albright, T. A., Hoffmann, R., and Kochi, J. K. (1977). The stability of organogold compounds. Hydrolytic, thermal, and oxidative cleavages of dimethylaurate(I) and tetramethylaurate(III). *Journal of the American Chemical Society*, 99(26):8440.
- Kopatzki, E. and Behm, R. J. (1991). STM imaging and local order of oxygen adlayers on Ni(100). *Surface Science*, 245(3):255–262.
- Landauer, R. (1957). Spatial Variation of Currents and Fields Due to Localized Scatterers in Metallic Conduction. *IBM Journal of Research and Development*, 1(3):223–231.
- Lee, J.-O., Lientschnig, G., Wiertz, F., Struijk, M., Janssen, R. A. J., Egberink, R., Reinhoudt, D. N., Hadley, P., and Dekker, C. (2003). Absence of Strong Gate Effects in Electrical Measurements on Phenylene-Based Conjugated Molecules. *Nano Letters*, 3(2):113–117.
- Lucas, A. A., Morawitz, H., Henry, G. R., Vigneron, J.-P., Lambin, P., Cutler, P. H., and Feuchtwang, T. E. (1988). Scattering-theoretic approach to elastic one-electron tunneling through localized barriers: Application to scanning tunneling microscopy. *Physical Review B*, 37(18):10708–10720.
- Mayne, A., Avery, A. R., Knall, J., Jones, T., Briggs, G., and Weinberg, W. (1993). An STM study of the chemisorption of C[2]H[4] on Si(001)(2 x 1). *Surface Science*, 284(3):247–256.
- Metzger, R. M., Chen, B., Höpfner, U., Lakshmikantham, M. V., Vuillaume, D., Kawai, T., Wu, X., Tachibana, H., Hughes, T. V., Sakurai, H., Baldwin, J. W., Hosch, C., Cava, M. P., Brehmer, L., and Ashwell, G. J.

- (1997). Unimolecular Electrical Rectification in Hexadecylquinolinium Tricyanoquinodimethanide. *Journal of the American Chemical Society*, 119(43):10455–10466.
- Miller, S. A., Turner, K. L., and MacDonald, N. C. (1997). Microelectromechanical scanning probe instruments for array architectures. *RSI*, 68(11):4155–4162.
- Mulliken, R. S., Rieke, C. A., and Brown, W. G. (1941). Hyperconjugation. *Journal of the American Chemical Society*, 63(1):41–56.
- Ness, H. and Fisher, A. J. (1997). Influence of the tip-induced electric field on the STM contrast of chemisorbed C₂H₄. *Physical Review B*, 55(15):10081–10093.
- Ohtani, H., Wilson, R. J., Chiang, S., and Mate, C. M. (1988). Scanning Tunneling Microscopy Observations of Benzene Molecules on the Rh(111)-(3 x 3)(C₆H₆ + 2CO) Surface. *Physical Review Letters*, 60(23):2398–2401.
- Perdew, J. P. and Zunger, A. (1981). Self-interaction correction to density-functional approximations for many-electron systems. *Physical Review B*, 23(10):5048–5079.
- Piccini, S., Selloni, A., Scandolo, S., Car, R., and Scoles, G. (2003). Electronic properties of metal-molecule-metal systems at zero bias: A periodic density functional study. *The Journal of Chemical Physics*, 119(13):6729–6735.
- Pople, J. A. (1977). *Applications of Electronic Structure Theory*, volume 4 of *Modern Theoretical Chemistry*, chapter 1, pages 1–27. Plenum Press, New York.
- Pople, J. A., Beveridge, D. L., and Dobosh, P. A. (1967). Approximate Self-Consistent Molecular Orbital Theory. V. Intermediate Neglect of Differential Overlap. *The Journal of Chemical Physics*, 47(2):2026–2033.
- Pople, J. A., Santry, D. P., and Segal, G. A. (1965). Approximate Self-Consistent Molecular Orbital Theory. I. Invariant Procedures. *The Journal of Chemical Physics*, 43:S129.
- Pople, J. A. and Segal, G. A. (1965). Approximate Self-Consistent Molecular Orbital Theory. II. Calculations with Complete Neglect of Differential Overlap. *The Journal of Chemical Physics*, 43:S136.

- Pople, J. A. and Segal, G. A. (1966). Approximate Self-Consistent Molecular Orbital Theory. III. CNDO Results for AB_2 and AB_3 Systems. *The Journal of Chemical Physics*, 44(3):3289–3296.
- Press, W. H., Flannery, B. P., Teukolsky, S. A., and Vetterling, W. T. (1999). *Numerical Recipes in C: The Art of Scientific Computing*. Cambridge University Press, Cambridge (U.K.), second edition.
- Reed, M. A., Zhou, C., Muller, C. J., Burgin, T. P., and Tour, J. M. (1997). Conductance of a Molecular Junction. *Science*, 278(5336):252–254.
- Reichert, J., Ochs, R., Beckmann, D., Weber, H. B., Mayor, M., and v. Löhneysen, H. (2002). Driving Current through Single Organic Molecules. *Physical Review Letters*, 88(17):176804–176807.
- Roothaan, C. C. J. (1951). New Developments in Molecular Orbital Theory. *Reviews of Modern Physics*, 23(2):69–89.
- Roshd, D. (1992). Theoretical interpretation of Scanning Tunneling Microscope studies of adsorbates. Master's thesis, University of Cambridge.
- Sautet, P. and Joachim, C. (1988a). Electronic interference produced by a benzene embedded in a polyacetylene chain. *Chemical Physics Letters*, 153(6):511–516.
- Sautet, P. and Joachim, C. (1988b). Electronic transmission coefficient for the single-impurity problem in the scattering-matrix approach. *Physical Review B*, 38(17):12238–12247.
- Sautet, P. and Joachim, C. (1988c). The switching ability of a three-level tight-binding system: the isolated and embedded case. *The Journal of Chemical Physics*, 21(21):3939–3957.
- Sautet, P. and Joachim, C. (1991). Calculation of the benzene on rhodium STM images. *Chemical Physics Letters*, 185(1-2):23–30.
- Scholz, M. and Köhler, H.-J. (1981). *Quantenchemische Nährungsverfahren und ihre Anwendung in der organischen Chemie*, volume 3 of *Quantenchemie*. Dr. Alfred Hüthig Verlag, Berlin. In German.
- Schuster, R., Barth, J. V., Ertl, G., and Behm, R. J. (1991). Phase transitions and domain-wall structures in the K/Cu(110) system: Scanning-tunneling-microscopy observations and Monte Carlo simulations. *Physical Review B*, 44(24):13689–13702.

- Seminario, J. M., Zacarias, A. G., and Darosa, P. A. (2001). Analysis of a dinitro-based molecular device. *The Journal of Chemical Physics*, 116(14):1671–1683.
- Slater, J. C. (1930). Atomic Shielding Constants. *Physical Review*, 36(1):57–64.
- Stewart, J. J. P. (1989a). Optimization of Parameters for Semi-Empirical Methods. I. Method. *Journal of Computational Chemistry*, 10:209.
- Stewart, J. J. P. (1989b). Optimization of Parameters for Semi-Empirical Methods. II. Applications. *Journal of Computational Chemistry*, 10:221–264.
- Szabo, A. and Ostlund, N. S. (1996). *Modern Quantum Chemistry*. Dover Publications, Inc. Mineola, New York.
- Taylor, J. R. (1972). *Scattering theory*. John Wiley & Sons, Inc., New York.
- Tersoff, J. and Hamann, D. R. (1983). Theory and Application for the Scanning Tunneling Microscope. *Physical Review Letters*, 50(25):1998–2001.
- Tersoff, J. and Hamann, D. R. (1985). Theory of the scanning tunneling microscope. *Physical Review B*, 31(2):805–813.
- Thomson, J. J. (1897). Cathode Rays. *Philosophical Magazine*, 44:293.
- Tromp, R. M., Hamers, R. J., and Demuth, J. E. (1985). Si(001) Dimer Structure Observed with Scanning Tunneling Microscopy. *Physical Review Letters*, 55(12):1303–1306.
- Tsukada, M., Kobayashi, K., and Ohnishi, S. (1990). First-principles theory of the scanning tunneling microscopy simulation. *Journal of Vacuum Science & Technology A*, 8(1):160–165.
- Tsukada, M., Kobayashi, K., Shima, N., and Isshiki, N. (1991). Scanning tunneling microscopy/scanning tunneling spectroscopy simulation of Si(111) $\sqrt{3}$ -B surface. *Journal of Vacuum Science & Technology B*, 9(2):492–494.
- Weiss, P. S. and Eigler, D. M. (1993). Site dependence of the apparent shape of a molecule in scanning tunneling microscope images: Benzene on Pt{111}. *Physical Review Letters*, 71(19):3139–3142.

- Wheland, G. W. (1941). The Resonance Energies of Unsaturated and Aromatic Molecules. *Journal of the American Chemical Society*, 63(7):2025–2027.
- Wolfsberg, M. and Helmholtz, L. (1952). The Spectra and Electronic Structure of the Tetrahedral Ions MnO_4^- , CrO_4^{--} , and ClO_4^- . *The Journal of Chemical Physics*, 20(1):837.
- Xue, X., Datta, S., and Ratner, M. A. (2001). Charge transfer and "band lineup" in molecular electronic devices: A chemical and numerical interpretation. *The Journal of Chemical Physics*, 115(9):4292–4299.
- Yourdshahyan, Y. and Rappe, A. M. (2002). Structure and energetics of alkanethiol adsorption on the Au(111) surface. *The Journal of Chemical Physics*, 117(2):825–833.
- Zeng, C., Li, B., Wang, B., Wang, H., Wang, K., Yang, J., Hou, J. G., and Zhu, Q. (2002). What can a scanning tunneling microscope image do for the insulating alkanethiol molecules on Au(111) substrates? *The Journal of Chemical Physics*, 117(2):851–856.
- Zülicke, L. (1973). *Grundlagen und allgemeine Methoden*, volume 1 of *Quantenchemie*. VEB Deutscher Verlag der Wissenschaften, Berlin. In German.
- Zülicke, L. (1985). *Atombau, chemische Bindung und molekulare Wechselwirkung*, volume 2 of *Quantenchemie*. Dr. Alfred Hüthig Verlag, Heidelberg. In German.

Danksagung

An erster Stelle möchte ich Prof. Ulrich Schollwöck danken. Er hatte die Idee, das Thema der vorliegenden Arbeit zu behandeln, gab entscheidende Hilfestellungen und Impulse während der Umsetzung des Vorhabens und ich verdanke ihm auch ungemein nützliche Kontakte, die er zu anderen Arbeitsgruppen geknüpft hat.

Xavier Bouju und Christian Joachim danke ich für ihre Einladung nach Toulouse und die freundliche Aufnahme in ihre Arbeitsgruppe während meines dortigen Aufenthalts.

Die Diskussionen mit Udo Beierlein und Christian Dupraz warfen wichtige Fragen auf, die zu beantworten Teil der vorliegenden Arbeit wurde. Es hat sich gelohnt, die Kooperation über den Rand des Fussballfeldes auf das Gebiet der Physik zu erweitern. Die Zusammenarbeit mit Prof. Bianca Hermann, aus einem CeNS Workshop hervorgegangen, hat schließlich dazu geführt, daß diese Arbeit auch einen Beitrag auf dem Gebiet leistet, das die ursprüngliche Motivation dargestellt hat. Leo Merz danke ich für die Daten, auf denen meine Berechnungen aufbauen.

Bei meinen jetzigen Zimmergefährten, Corinna Kollath und Dominique Gobert, möchte ich mich für ihre netten Ablenkungen bedanken. Insbesondere Dominique danke ich für die Zeit, die er sich zum Korrekturlesen dieser Arbeit genommen hat. Ebenso danke ich Michael Sindel für seine Anregungen. Prof. Jan von Delft und allen Mitarbeitern, Doktoranden und Diplomanden seines Lehrstuhls danke ich für die schöne Zeit dort.

Bei Herrn Prof. Wagner bedanke ich mich dafür, daß ich lange Jahre die sehr nette Atmosphäre an seinem Lehrstuhl genießen durfte. Dieser Dank gilt somit natürlich auch den ehemaligen Mitarbeitern, insbesondere Sigmund Stintzing, Claus Beisbart, Jens Schmalzing und Patrick Werner.

Schließlich möchte ich meinem Großvater danken, denn ohne ihn wären wohl manche Pfade in meinem Leben weniger glücklich verlaufen.

Ganz zum Schluß geht mein Dank an Carola Weiß mit dem Versprechen, daß wir die ganzen der Arbeit zum Opfer gefallenen Urlaube jetzt nachholen werden!

